PCCP

View Online
Dynamic Article Links

Cite this: *Phys. Chem. Chem. Phys.*, 2011, **13**, 10593–10616

www.rsc.org/pccp

PERSPECTIVE

In silico screening of metal–organic frameworks in separation applications†

Rajamani Krishna and Jasper M. van Baten

Received 1st February 2011, Accepted 5th April 2011
DOI: 10.1039/c1cp20282k

Porous materials such as metal–organic frameworks (MOFs) and zeolitic imidazolate frameworks (ZIFs) offer considerable potential for separating a variety of mixtures such as those relevant for CO_2 capture (CO_2/H_2, CO_2/CH_4, CO_2/N_2), CH_4/H_2, alkanes/alkenes, and hydrocarbon isomers. There are basically two different separation technologies that can be employed: (1) a pressure swing adsorption (PSA) unit with a fixed bed of adsorbent particles, and (2) a membrane device, wherein the mixture is allowed to permeate through a micro-porous crystalline layer. In view of the vast number of MOFs, and ZIFs that have been synthesized there is a need for a systematic screening of potential candidates for any given separation task. Also of importance is to investigate how MOFs and ZIFs stack up against the more traditional zeolites such as NaX and NaY with regard to their separation characteristics. This perspective highlights the potency of molecular simulations in determining the choice of the best MOF or ZIF for a given separation task. A variety of metrics that quantify the separation performance, such as adsorption selectivity, working capacity, diffusion selectivity, and membrane permeability, are determined from a combination of Configurational-Bias Monte Carlo (CBMC) and Molecular Dynamics (MD) simulations. The practical utility of the suggested screening methodology is demonstrated by comparison with available experimental data.

1. Introduction

With the recent advances in reticular chemistry, there has been considerable research on the development of novel porous materials such as metal–organic frameworks (MOFs),[1] zeolitic imidazolate frameworks (ZIFs),[2,3] and covalent organic frameworks (COFs).[4] MOFs, ZIFs, and COFs offer considerable potential for application in wide variety of applications that include storage, separations and catalysis.[5–12] In comparison to traditionally used porous materials such as zeolites, these novel materials offer significantly higher surface areas and porosities. This is underscored in the data presented in Fig. 1 for surface areas and pore volumes of some representative zeolites, MOFs and ZIFs. The commonly used zeolite, FAU, for example, has a characteristic size (window aperture) of 7.4 Å, a pore volume of 0.33 $cm^3\ g^{-1}$, and a surface area of 980 $m^2\ g^{-1}$. The accessible pore volumes of MOFs are commonly in the 0.5–2 $cm^3\ g^{-1}$ range. Furthermore, significantly higher surface areas are available with MOFs; for example MOF-177 has an area of 4800 $m^2\ g^{-1}$. The pore dimensions of MOFs are also often significantly larger; MgMOF-74 has one-dimensional hexagonal-shaped channels of approximately 11 Å diameter.

The focus of this perspective is on the use of MOFs and ZIFs in a variety of separation applications. A substantial amount of the published research on MOFs is dedicated to the issue of CO_2 capture by selective adsorption.[11–15] Three CO_2 separation issues are considered to hold the greatest promise for reducing CO_2 emissions. Firstly, we have the problem of separating CO_2 and N_2 from power plant flue gas streams; this is also termed post-combustion processing. Secondly, in pre-combustion processing of syngas mixtures, CO_2 and H_2 need to be separated. Thirdly, there is the issue of sweetening of sour natural gas, involving separation of CO_2 and CH_4. For CO_2 capture, ordered crystalline microporous adsorbent materials offer energy efficient alternatives to more conventional separation techniques such as amine absorption.[14–21] The traditional choices of adsorbent materials are cation-exchanged zeolites such as NaX and NaY that offer high separation

Van't Hoff Institute for Molecular Sciences, University of Amsterdam, Science Park 904, 1098 XH Amsterdam, The Netherlands.
E-mail: r.krishna@uva.nl; Fax: +31 20 525 5604;
Tel: +31 20 627 0990

† Electronic supplementary information (ESI) available: (a) The pore landscapes, and structural details of a variety of micro-porous structures (zeolites, MOFs, ZIFs) referred to in this article, along with force fields, and simulation methods. (b) Snapshot showing the location of molecules within the structures. (c) Simulation results for mixture adsorption, diffusion, and permeation for all of the guest–host combinations. (d) Video animations obtained from MD simulations for diffusion of CO_2/CH_4 mixture in AFX, CO_2/H_2 mixture in MgMOF-74, CH_4/H_2 mixture in MgMOF-74, CO_2/CH_4 mixture in LTA, and the framework dynamics of ZIF-8. See DOI: 10.1039/c1cp20282k

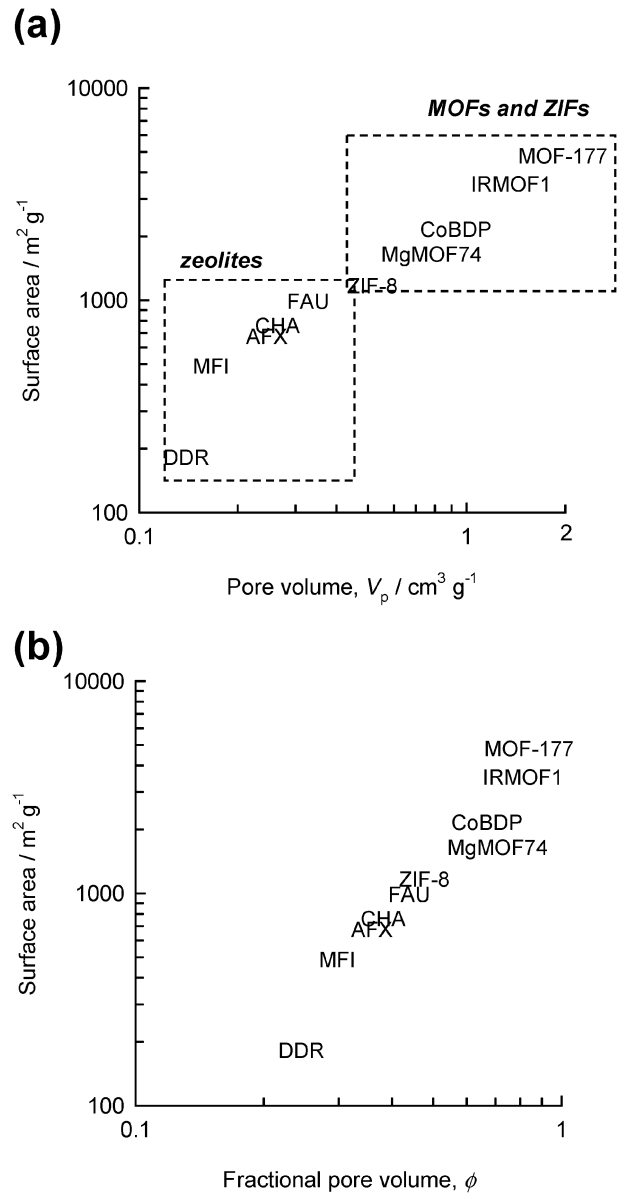

Fig. 1 Data on surface area *vs.* (a) pore volume, V_p, and (b) fractional pore volume, ϕ, for some representative zeolites, MOFs and ZIFs. The data are obtained using the simulation methodology described in the ESI.†

selectivities.[15,18] Due to their higher surface areas and pore volumes, there are significant advantages in the use of MOFs and ZIFs, in comparison to NaX and NaY, with respect to adsorption *capacity*. Using MOFs, a wide variety of strategies can be adopted to enhance the CO_2 selectivity; these include appropriate choice of ligand design,[22] the introduction of non-framework cations,[23,24] use of exposed metal cation sites,[25–29] and post-synthetic modification by introduction of polar surface groups.[30] The adsorption selectivities are also enhanced by incorporation of special functional groups within a framework.[31–39] For example, Couck *et al.*[37] demonstrated that functionalizing the MIL-53(Al) framework with amino groups increases its selectivity in CO_2/CH_4 separations by orders of magnitude while maintaining a very high capacity for CO_2 capture.

Besides CO_2 capture, MOFs and ZIFs have potential use in separating a variety of other mixtures, including CH_4/H_2,[15,40–44] alkane/alkene,[45–47] linear alkanes,[48] linear alcohols,[49] alkane isomers,[50–54] xylenes,[8,48,55–57] and removal of toxic gases.[58]

For any given mixture separation there is a vast number of candidate MOF and ZIF structures that may be suitable for technological applications. A pressure swing adsorption (PSA) unit with a fixed bed of adsorbent particles is often the technology of choice. An alternative is to use a membrane device, wherein the mixture is allowed to permeate through a micro-porous crystalline layer, with a thickness of a few micro-metres.[47,59] There is a need to adopt a systematic procedure for selecting the "best" structure for use in either PSA or membrane units. Also of importance is to investigate how MOFs and ZIFs stack up against the more traditional zeolites such as NaX and NaY with regard to their separation characteristics. Most of the published screening methodologies for adsorbents are on the basis of the adsorption selectivity, S_{ads}, defined for separation of a binary mixture of species 1 and 2 by

$$S_{ads} = \frac{q_1/q_2}{f_1/f_2} \qquad (1)$$

where the q_i represents the component molar loading in equilibrium with a bulk fluid phase with partial fugacities f_i. We choose to use fugacities, f_i, in eqn (1) instead of partial pressures because in many CO_2 separation applications the pressures encountered are high, in the 1–10 MPa range, and thermodynamic non-idealities are non-negligible.

Palomino *et al.*[60] and Bao *et al.*,[18] for example, have compared the CO_2/CH_4 adsorption selectivity for various MOFs with cation-exchanged zeolites. In the study of Bao *et al.*,[18] the S_{ads} value for MgMOF-74 was found to be comparable to that of NaX zeolite.

Besides S_{ads}, another important factor that determines the economics of PSA units is the working capacity, or "delta loading", Δq.[16,20,29,61] This metric is defined as the difference in the loadings of the component that needs to be preferentially adsorbed, expressed in mol per kg of microporous crystalline material, at the "adsorption" pressure minus the corresponding loading at the "desorption", or purge, pressure. The adsorption pressure could be in the 0.1–10 MPa range, and the desorption pressure could be in the 0.01–0.1 MPa range. Based on a careful analysis of the variety of factors that affect PSA performance, Kumar[62] concluded that neither highest S_{ads} nor maximum Δq on its own can be chosen as the criterion for adsorbent selection; rather, it is the combination of S_{ads} and Δq which leads to the best adsorbent. Krishna and Long[61] have shown that breakthrough times in a PSA unit are influenced by both S_{ads} and Δq. A shorter breakthrough time implies that more frequent regeneration is necessary. Ho *et al.*[16] have clearly demonstrated that both S_{ads} and Δq determine the efficacy and cost of CO_2 capture in a PSA unit. One important advantage of the higher surface areas of MOFs is that the working capacity is expected to be significantly higher than for zeolites, as we shall demonstrate later in this article. For high pressure PSA operations, the capacity limitations of traditional adsorbents such as NaX and LTA-5A will result in shorter breakthrough times, and poorer PSA performance compared to MOFs.[61]

For membrane separation devices the two important characteristics are the (1) permeation selectivity, S_{perm}, defined by

$$S_{perm} = \frac{N_1/N_2}{f_1/f_2} \quad (2)$$

and (2) the permeability, Π_i, of the species that needs to be preferentially removed

$$\Pi_i = \frac{N_i}{\Delta f_i/\ell} \quad (3)$$

In eqn (2) and (3), N_i are the permeation fluxes, ℓ is the thickness of the microporous crystalline layer, and Δf_i is the difference in the partial gas phase fugacities f_i between the upstream and downstream membrane compartments.

The permeation selectivity can be expressed as the product[15]

$$S_{perm} = S_{ads} \times S_{diff} \quad (4)$$

As an approximation, the diffusion selectivity can be expressed as the ratio of the self-diffusivities of the permeating species in the mixture[15]

$$S_{diff} = \frac{D_{1,self}}{D_{2,self}} \quad (5)$$

Eqn (5) holds in cases where the concentration within the pores is not near saturation values. The more general, and correct, method of calculation of the diffusion selectivities relies on the use of the Maxwell–Stefan equations;[15,63–66] see ESI† for further details. For membrane devices *both* adsorption *and* diffusion characteristics are important in determining the separation performance.[15,63,67–69] This is in contrast with PSA units, for which diffusional aspects are quite often irrelevant, except in processes such as N_2/O_2 separations that additionally rely on diffusional effects.[67] Due to the larger pore volume, and channel dimensions of many MOFs, we should expect the permeability Π_i to be significantly higher than for zeolites.

Experimental screening of potential candidate structures for use in PSA and membrane devices is very time consuming. An alternative approach, as underlined in several recent investigations, is to harness the power of molecular simulation techniques.[15,21,28,42,43,63,70–80] With the significant advances in the development of molecular simulation techniques, the adsorption and diffusion characteristics of porous materials can be determined reasonably accurately. This opens up the possibility of *in silico* screening of ordered crystalline nanoporous structures that offer the optimum separation characteristics.[15] Molecular simulations can be very useful in narrowing down the choices to a handful of promising structures than can be subsequently subjected to more thorough experimental investigations.

The primary objective of this perspective is to demonstrate the potency of molecular simulations in calculating the parameters S_{ads}, Δq, S_{diff}, S_{perm}, and Π_i that determine the separation performance of PSA and membrane devices. For illustration purposes we consider the task of separating the following mixtures: CO_2/CH_4, CO_2/N_2, CO_2/H_2, CH_4/H_2, and *n*-hexane/2-methylpentane/3-methylpentane/2,2-dimethylbutane/2,3-dimethylbutane. Specifically, we demonstrate the power of molecular simulations to screen a large number of MOFs, ZIFs and zeolites for each of these chosen mixtures. The MOFs and ZIFs were chosen to represent a wide variety of metal atoms, organic linkers and pore topologies, and include MgMOF-74 (=Mg_2(dobdc)),[25,26,28,81–83] ZnMOF-74 (=Zn_2(dobdc)),[25,26,28,81] MOF-177,[84] CuBTC,[85] IRMOF-1,[86,87] MIL-53(Cr)-lp,[88] MIL-47,[89–91] Zn(bdc)dabco,[92,93] *rho*-ZMOF,[24] CuBTT,[36] BeBTB,[94] Co(BDP),[95,96] and ZIF-8.[3] As illustration, the frameworks for two of these structures, MOF-177 and MgMOF-74, are shown in Fig. 2. Additionally, several commonly used zeolites (AFX, BEA, BOG, CHA, DDR, ERI, MFI, FAU, NaX, NaY, LTA–Si, ITQ-29) were

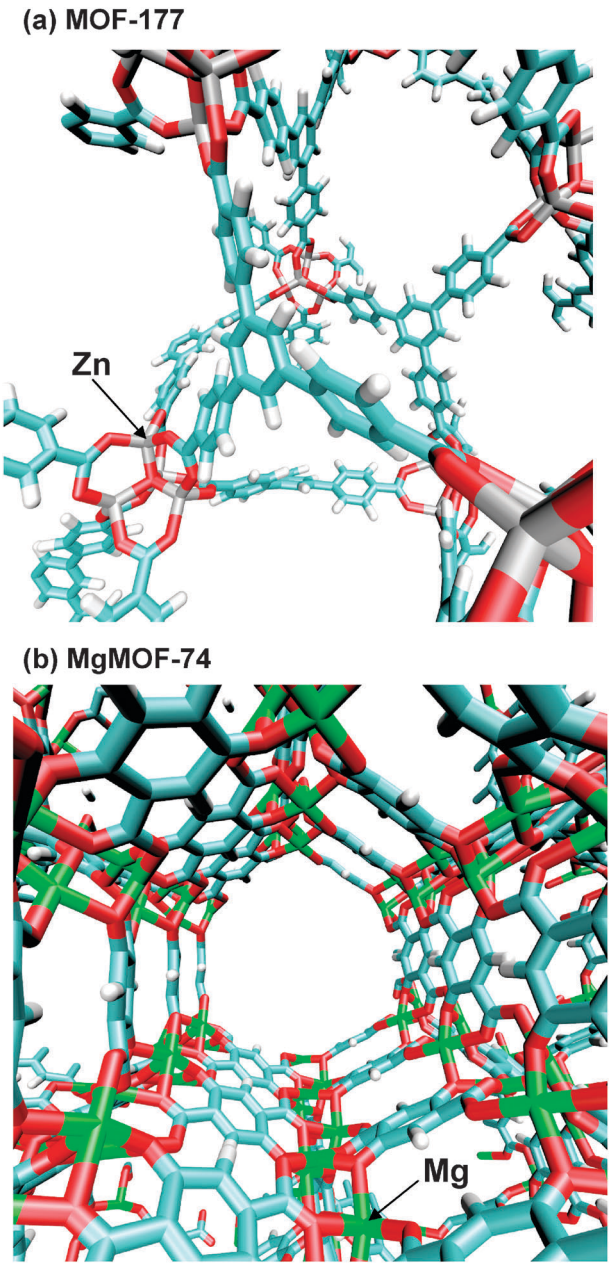

Fig. 2 (a) Structure of MOF-177 = $Zn_4O(BTB)_2$ with (BTB^{3-} = 1,3,5-benzenetribenzoate). (b) Structure of MgMOF-74 = Mg_2(dobdc) with dobdc = ($dobdc^{4-}$ = 1,4-dioxido-2,5-benzenedicarboxylate). Note that the Mg atoms are "open" in the sense that these are easily accessible to guest molecules.

investigated for comparison purposes; the structural details of the chosen zeolite structures are obtained from the website of the International Zeolite Association (IZA).[97] With the exception of NaY and NaX, all the zeolites considered in this work are all-silica versions. In all cases, we determined S_{ads} and Δq by use of Configurational-Bias Monte Carlo (CBMC) simulations of mixture adsorption. The parameters S_{diff} and Π_i were determined using Molecular Dynamics (MD) simulations of mixture diffusion. For further theoretical background to the simulation techniques used, the reader is referred to published articles[63,98–104] and books.[76,105–107]

For the simulations involving zeolites, force fields used are those from the published literature; these have been developed on the basis fitting to a large body of experimental isotherm data.[98,108–111] For MOF and ZIF simulations, the available force fields are very limited in number. Therefore, the guest-framework van der Waals dispersion interactions were estimated on the basis of the UFF[112] and DREIDING[113] force fields for the framework atoms. The major issue for simulations involving CO_2 bearing mixture relates to the calculation of the electrostatic interactions between CO_2 and the framework atoms. For very limited number of structures, the framework charges have been estimated from density functional theory and quantum chemical calculations.[24,28,114–116] In cases where such information on charges is not available, one approach is to use group-contribution procedures, that have been developed on the basis of quantum chemical calculations of a large number of frameworks.[117,118]

In performing molecular simulations, we assume perfect, defect-free crystals, and rigid crystalline frameworks. These assumptions are considered to be reasonable for purposes of screening, the focus of the current study. However, for more accurate design purposes, it may be necessary to take other factors into consideration, such as surface resistance or inter-crystalline resistance of crystals,[119,120] and framework flexibility influences.[121–125] The influence of framework flexibility on the hopping of guest molecules across the narrow windows of CHA, DDR, LTA, and ZIF-8 is discussed in the literature.[126,127] In MOFs such as MIL-53, guest-induced structural transformations may occur, and this needs special analysis.[125,128]

The ESI† accompanying this publication gives information on the specific force fields used, details of the micro-porous structures investigated (unit cell dimensions, accessible pore volume, characteristic pore dimensions), CBMC and MD simulation methodologies, pore landscapes and snapshots, along with the data base of simulation data on mixture isotherms.

2. Screening of adsorbents for CO_2/CH_4, CO_2/N_2, CO_2/H_2, and CH_4/H_2 mixture separations in PSA units

We start by considering the separation of mixtures that are relevant for CO_2 capture. For CO_2/CH_4, CO_2/N_2, and CO_2/H_2 mixtures, Fig. 3a–c present data on the S_{ads} as a function of the total gas phase fugacity, $f_t = f_1 + f_2$, for a sample of the wide variety of microporous structures investigated. CO_2 has a larger quadrupole moment (14.3×10^{-40} C m^2) and a higher polarizability (26.3×10^{-25} cm^3) than each of the partner molecules H_2, CH_4, and N_2. Consequently, CO_2 has the higher adsorption strength in all three mixtures. There are several points that are noteworthy. Firstly, we note that the adsorption selectivity of CO_2 with respect to its partner molecule is higher in cases where the structure contains non-framework cations such as Na^+; the high values of S_{ads} for NaX and NaY can be ascribed to the strong electrostatic interactions between the CO_2 and the non-framework cations as has been underlined in the literature.[15,23,75,129] In the case of *rho*-ZMOF, S_{ads} values higher than 50 for CO_2/H_2, CO_2/CH_4, and CO_2/N_2 adsorption are due both to electrostatic interactions of CO_2 with the charges of the anionic framework atoms and charge-balancing extra-framework Na^+ ions.[24] It is also noteworthy that MOFs such as MgMOF-74 (*cf.* Fig. 2b) and ZnMOF-74, with exposed metal cation sites,[25,26] also exhibit high selectivities in favor of CO_2, that are comparable with those obtained with *rho*-ZMOF. For all three mixtures, the S_{ads} value is significantly higher for MgMOF-74 when compared to ZnMOF-74; this is because of stronger binding energy of CO_2 with the Mg^{++}, as compared to Zn^{++}.[28]

Of the wide variety of all-silica zeolites that were investigated, it is remarkable that AFX exhibits S_{ads} values that are comparable to, and in some cases higher than that of NaX, NaY, *rho*-ZMOF and MgMOF-74. The statement of Babarao and Jiang[24] in their paper "The predicted selectivities in *rho*-ZMOF are the highest reported to date among various MOFs and unprecedentedly higher than those for other porous materials" needs to be revised in light of the data presented in Fig. 3. In order to understand the reasons for the high selectivities exhibited by AFX, we need to examine the pore landscapes as shown in Fig. 4. In one unit cell of AFX there are 4 cages and 4 small pockets. The 8-ring windows separating two cages are 3.44 Å × 3.88 Å in size. The window regions and the small pockets are preferred locations for CO_2;[130,131] the pockets can be viewed as providing an "egg-carton" structure. CH_4, N_2, or H_2 do not prefer to locate at the window regions, and are preferentially located within the cages. Since there are 12 windows per unit cell of AFX, the adsorption selectivity for CO_2 is exceptionally high. However, the diffusion of CO_2 in and out of the pockets is a very slow process. This can be appreciated by viewing the animations of MD simulations of CO_2/CH_4 mixture diffusion in AFX, that is available as ESI.† Due to the slow diffusion of CO_2 it is likely that the CO_2 ensconced in the pockets are practically stagnant, and the high selectivities predicted by CBMC simulations may not be realizable in practice. The preferential perching of CO_2 in the window regions separating cages also explains the high values of S_{ads} found for CHA.[64,130,132] Other all-silica zeolites such as BIK and JBW also offer egg-carton structures for CO_2, but these structures have very low working capacities and are not suitable for practical use as adsorbents; see ESI† for further information. In this context, it is worth stressing that many microporous structures contain channels, pockets or cages that are not accessible in experiments. In CBMC simulations, it is important to block such regions in order to obtain a fair representation of experimental reality.[79] For example, the sodalite cages in LTA, ITQ-29, FAU, TSC need to be blocked as these are inaccessible to guest molecules.

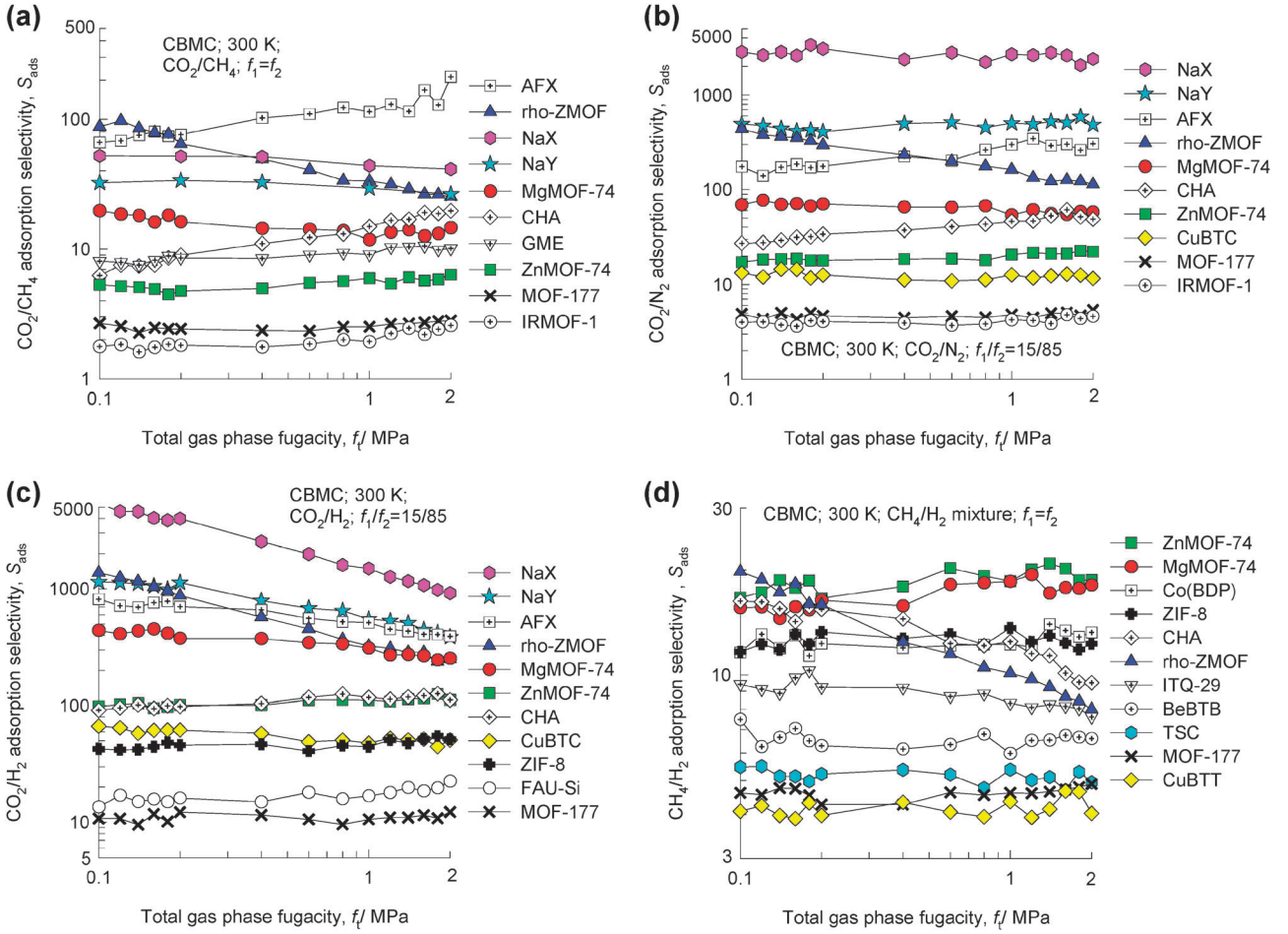

Fig. 3 Adsorption selectivities, S_{ads}, for (a) CO_2/CH_4 (b) CO_2/N_2, (c) CO_2/H_2, and (d) CH_4/H_2 mixtures at 300 K in a variety of MOFs and zeolite structures, obtained from CBMC simulations. In (a) and (d) the partial fugacities in the gas phase are equal, *i.e.* $f_1 = f_2$. In (b) and (c) the gas phase partial fugacities satisfy $f_1/f_2 = 15/85$. For clarity of presentation only a selection of the simulation data are presented here; the complete set of data are available as ESI.†

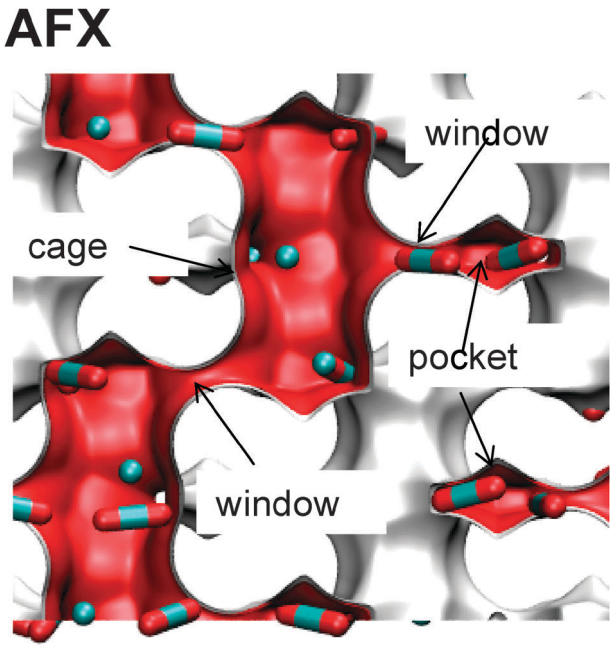

Fig. 4 Pore landscape of AFX, showing the location of CO_2 and CH_4 molecules.

Also, DDR zeolite contains pockets that need blocking.[79,133] The molecular simulation screening study of Liu and Smit[129] must be treated with caution because the inaccessible pockets of LTA and DDR were not blocked.[79] There are two sizes of channels within ZIF-68, and it is not entirely evident that the narrower channels are accessible to all except very small molecules. The molecular simulation results of Liu and Smit[134] for ZIF-68, obtained without adopting any blocking strategy, need to be re-assessed. There area inaccessible pockets in *rho*-ZMOF that need to be blocked (see ESI† for blocking information), while it is to be noted that Babarao and Jiang[24] did not employ any blocking strategy.

Additionally, we investigated the separation of CH_4/H_2 mixtures, that is of relevance in the process of purification of synthesis gas obtained from steam reforming of natural gas.[42,43] The data on adsorption selectivities for CH_4/H_2 mixtures are shown in Fig. 3d. In this case, electrostatic interactions are not of relevance. The best selectivities are obtained with MOFs with exposed metal cation sites: MgMOF-74 and ZnMOF-74. The molecular simulation studies of Gallo and Glossman-Mitnik[43] and Keskin[42] had concluded, respectively, that ZnMOF-74 and CoMOF-74

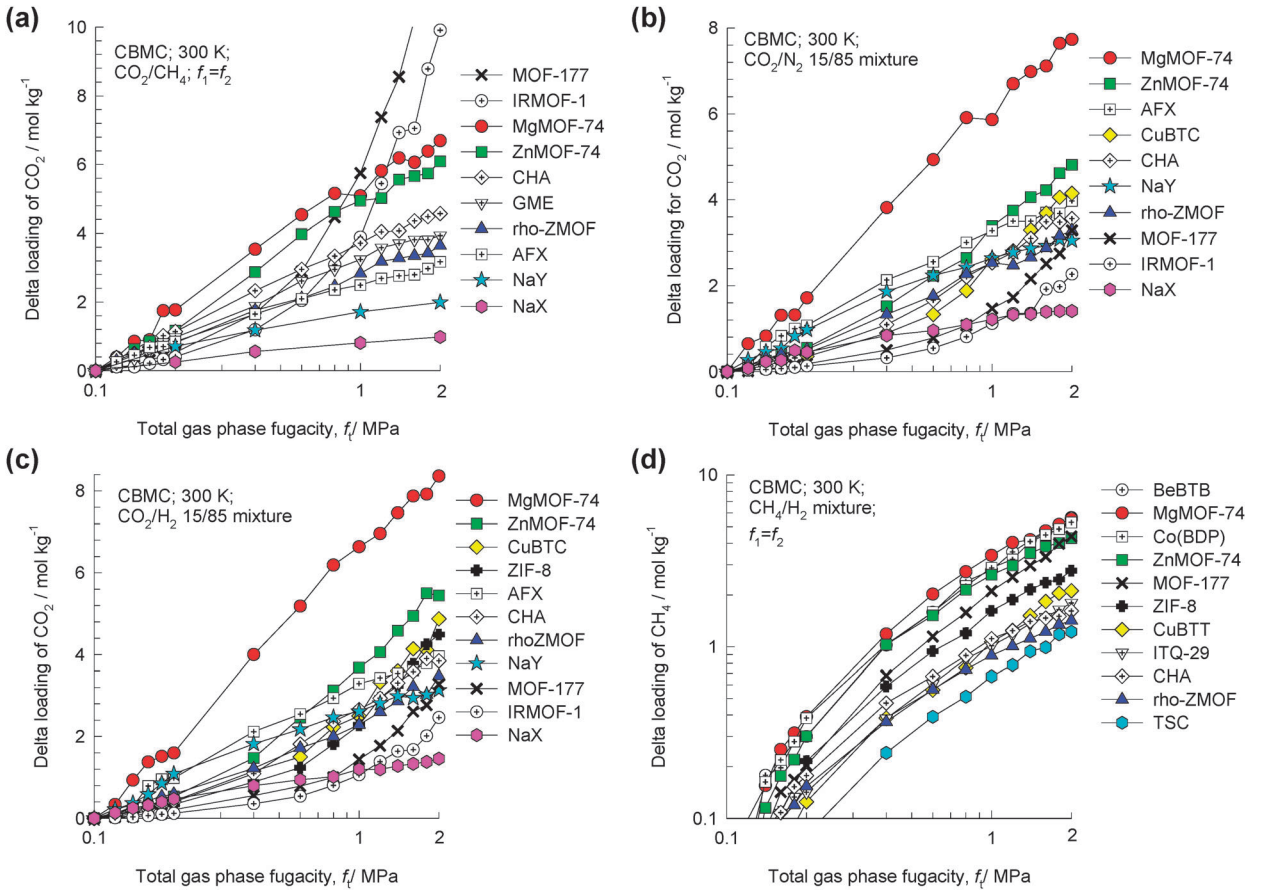

Fig. 5 Delta loadings, Δq, for (a) CO_2/CH_4 (b) CO_2/N_2, (c) CO_2/H_2, and (d) CH_4/H_2 mixtures at 300 K in a variety of MOFs and zeolite structures, obtained from CBMC simulations. For calculations of Δq, the desorption pressure is assumed to be 0.1 MPa. For clarity of presentation only a selection of the simulation data are presented here; the complete set of data are available in the ESI.†

yield the highest S_{ads} values for CH_4/H_2 separation, but neither paper had evaluated the performance of MgMOF-74.

Fig. 5a–d present data on the working capacities, Δq, as a function of the total bulk gas phase fugacity, f_t. Generally speaking, more open MOF structures with high pore volumes, V_p, and high surface areas tend to yield high working capacities. This is evidenced by the fact that structures such as MgMOF-74, ZnMOF-74, MOF-177, and BeBTB yield the highest values of Δq. These results underline the fact that the major advantage of using MOFs is to be found in their higher working capacity. Broadly speaking, MOFs have a higher surface areas and pore volumes than zeolites (*cf.* Fig. 1), and therefore have significantly higher values of Δq. A further point to note is that structures such as MOF-177 and BeBTB have very extremely low framework densities, and consequently the volumetric capacity expressed in terms of moles adsorbed per m^3 of framework will be significantly lowered. The recent work of Herm *et al.*[29] has demonstrated that for high pressure separation of CO_2/H_2 mixtures MOF-177 and BeBTB have higher capacities when compared to NaX zeolite, even on a volumetric basis.

Since both S_{ads} and Δq govern the costs of separation in a PSA unit, Fig. 6a–d present comparisons of S_{ads} *versus* Δq values for the four different mixtures, for an arbitrarily chosen total gas phase fugacity of 1 MPa and a desorption pressure of 0.1 MPa. The most desirable structures should be in the top right hand corner of the S_{ads} *vs.* Δq plots. Our molecular simulations clearly demonstrate the drawbacks of the commonly used adsorbents such as NaX and NaY; these have high CO_2 selectivities but relatively low working capacities. Of all the MOFs considered here, MgMOF-74 offers the best *combination* of S_{ads} and Δq values. Except in the case of CO_2/CH_4 mixtures, the S_{ads} is found to be higher than about 100, making it very attractive for technological exploitation.

3. Comparing molecular simulation data with experimental data on adsorption in MOFs

Since the good performance of MgMOF-74 is largely attributable to the strong CO_2 adsorption capability, we now seek experimental verification of the accuracy of the molecular simulations. In Fig. 7a we compare the experimentally measured CO_2 isotherm at 298 K, measured experimentally by Dietzel *et al.*[83] with CBMC simulations. The experimental data show an inflection at a loading of one molecule of CO_2 per atom of Mg in the framework. We note that for pressures exceeding 0.1 MPa, there is good agreement between the CBMC simulations and experiment. However, for pressures below 0.1 MPa, the experimental loadings are significantly higher than the simulated values. The reason for this deviation

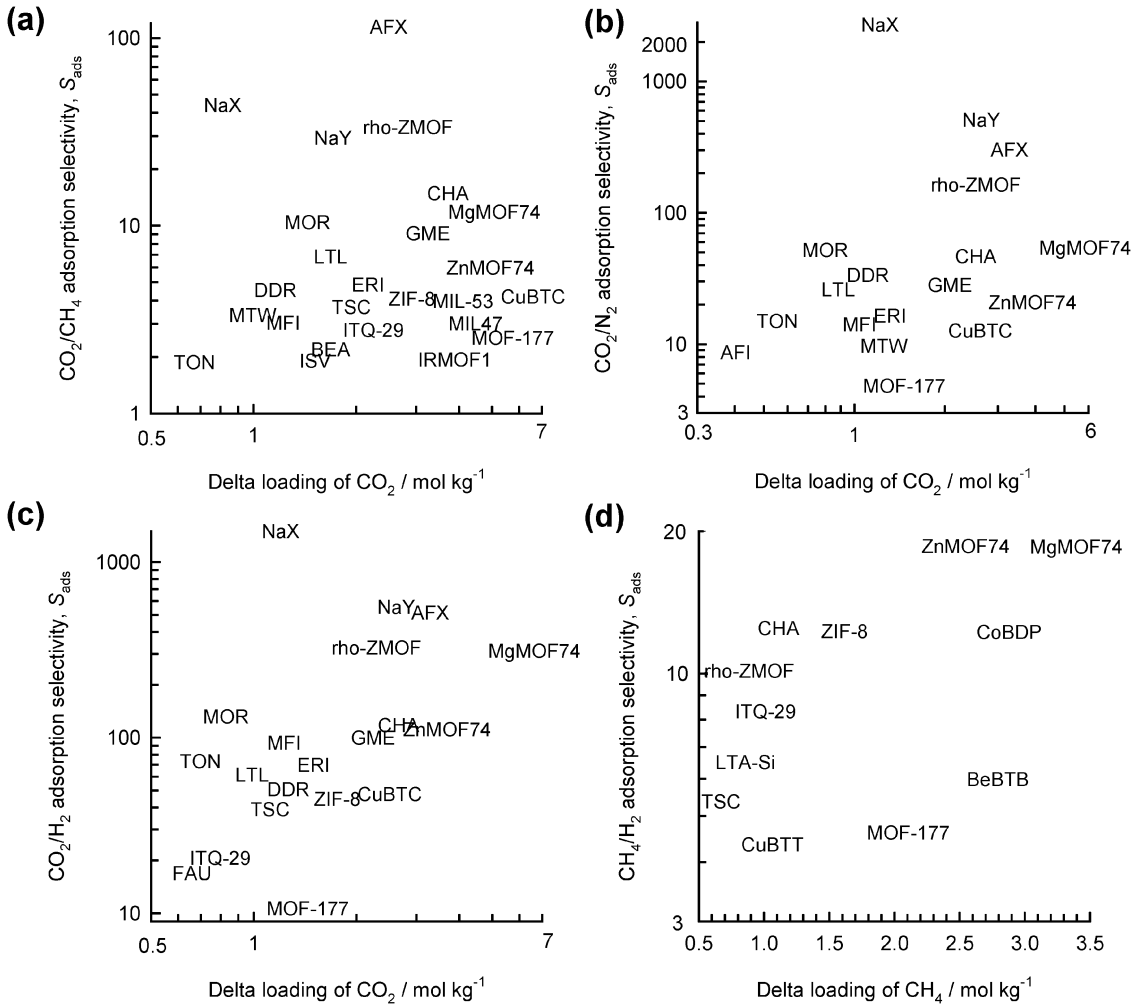

Fig. 6 Adsorption selectivities, S_{ads}, *vs.* delta loadings, Δq, for (a) CO_2/CH_4 (b) CO_2/N_2, (c) CO_2/H_2, and (d) CH_4/H_2 mixtures at 300 K in a variety of MOFs and zeolite structures. The chosen conditions correspond to an "adsorption" fugacity f_t = 1 MPa, and "desorption" fugacity = 0.1 MPa. For clarity of presentation only a selection of the simulation data is presented here; the complete set of data are available in the ESI.†

can be traced to the fact that our force field implementation, following the work of Yazaydin *et al.*,[28] does not explicitly account for orbital interactions and polarization. Such effects are particularly strong in the low pressure region; the influence of polarization is of lesser importance at higher pressures.

The implications of the data presented in Fig. 7a are that the S_{ads} values obtained from CBMC simulations for MgMOF-74 are most likely to be conservative in the Henry regime at $f_t < 0.1$ MPa. To confirm this, we present in Fig. 7b the data on the S_{ads} for CO_2/CH_4 mixtures reported in the experimental study of Bao *et al.*;[18] their calculations were carried out on the basis of fits of their experimental pure component isotherm data in the Henry regime for either component in the mixture. Fig. 7b also shows the corresponding S_{ads} from CBMC mixture simulations. While the CBMC simulations predict a S_{ads} value of about 20, the estimations on the basis of the experimental data are considerably higher and in the range of 40–200. An important consequence is that the adsorption selectivities for MgMOF-74 in post-combustion CO_2 capture from CO_2/N_2 mixtures, that is usually operated at CO_2 partial pressures of about 0.02–0.04 MPa range, can be expected to be significantly higher than those predicted from CBMC simulations.

We now address the issue of estimation of S_{ads} for binary mixtures using pure component isotherm data. Such estimations are essential in practice because experimental data on mixture adsorption is time consuming and extremely rare in practice.[135] The commonly used approach is to use the Ideal Adsorbed Solution Theory (IAST) of Myers and Prausnitz.[136] In applying the IAST, it is necessary to have reliable fits of the pure component isotherm data over the wide range of pressures. The isotherm model should be capable of capturing the inflection characteristics such as that observed for CO_2 in MgMOF-74; see Fig. 7a. Such inflection behavior can be captured by using the dual-site Langmuir–Freundlich isotherm

$$q_i = q_{i,A,sat}\frac{b_{i,A}f_i^{\nu_{i,A}}}{1+b_{i,A}f_i^{\nu_{i,A}}} + q_{i,B,sat}\frac{b_{i,B}f_i^{\nu_{i,B}}}{1+b_{i,B}f_i^{\nu_{i,B}}} \qquad (6)$$

The continuous solid and dashed lines in Fig. 7a are the fits of the CBMC and Dietzel experimental isotherm data in which

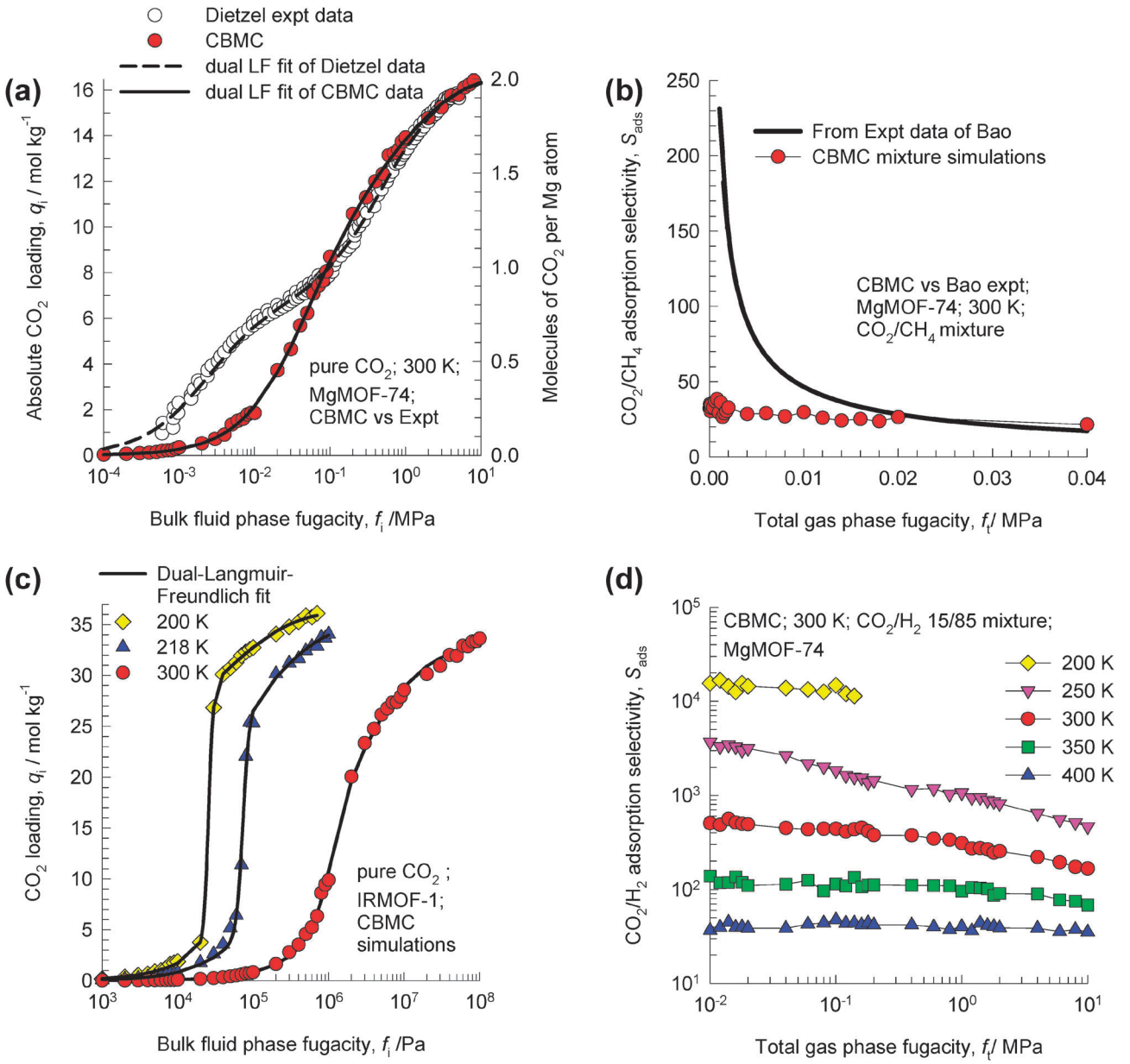

Fig. 7 (a) Pure component isotherm for CO_2 in MgMOF-74. Comparison of experimental data of Dietzel *et al.*[83] at 298 K with CBMC simulation data at 300 K. The published experimental data of Dietzel *et al.* are given in terms of excess loadings; these have been converted to absolute loadings by estimating the fluid densities within the pores using the Peng–Robinson equation of state. The experimental data on pore volume, 0.63 $cm^3\ g^{-1}$, were used in this conversion. The continuous solid and dashed lines are the fits of the CBMC simulated data using the dual-site Langmuir–Freundlich isotherm. (b) Comparison of S_{ads} data for CO_2/CH_4 mixture reported in the experimental study of Bao *et al.*[18] with CBMC simulated data. (c) CBMC simulations of pure component isotherms for CO_2 adsorption in IRMOF-1 at 200 K, 218 K, and 300 K. Also shown are the fits using eqn (6). (d) Comparison of CBMC simulated S_{ads} data for CO_2/H_2 mixture adsorption in MgMOF-74 at various temperatures plotted against the total gas phase fugacity, f_t.

all the six constants in eqn (6) were fitted to match the data points; neither exponent $\nu_{i,A}$ nor $\nu_{i,B}$ was restricted to unity. For CO_2 adsorption in MOFs and zeolites, it is essential to use eqn (6) for isotherm fitting in order to capture some of the essential characteristics such as cluster formation.[52,131,133] The critical temperature of CO_2 is 301 K, and there is a significant amount of cluster formation for adsorption at temperatures lower than 300 K. Due to cluster formation the isotherms become increasingly steeper as the temperature is lowered; this is witnessed in CBMC simulations for CO_2 isotherms in IRMOF-1 for 200 K, 218 K, and 300 K; see Fig. 7c. The steepness of the isotherms can only be properly captured provided at least one of the exponents ν_i exceeds unity. One consequence of the decrease in the degree of clustering of CO_2 with increasing temperature is that S_{ads} decreases with increasing T; this is demonstrated in Fig. 7d by CBMC simulations of S_{ads} for CO_2/H_2 mixtures in MgMOF-74 at different temperatures. It is noteworthy that the S_{ads} at 300 K is about two orders of magnitude lower than that at 200 K; this lowering cannot be easily rationalized without considering

clustering effects. Care should therefore be exercised when extrapolating information on adsorption selectivities obtained at a certain temperature to other values of T. Yang *et al.*[80] have illustrated the possibility of enhancing S_{ads} by choosing framework atoms that lead to steep CO_2 isotherms.

Fig. 8 presents a comparison of the IAST predictions with the CBMC simulation data for component loadings in (a) CO_2/N_2 and (b) CO_2/H_2 mixtures. We see excellent agreement of the IAST with CBMC data; this confirms the applicability of IAST for practical purposes. Similar good agreement was earlier established for adsorption of a wide variety of mixtures in different zeolites.[74,137] An important consequence is that for practical purposes we may estimate S_{ads} and Δq using *pure* component isotherm data. We believe this procedure to be accurate enough for practical design purposes, except when severe clustering of guest molecules occurs.[133]

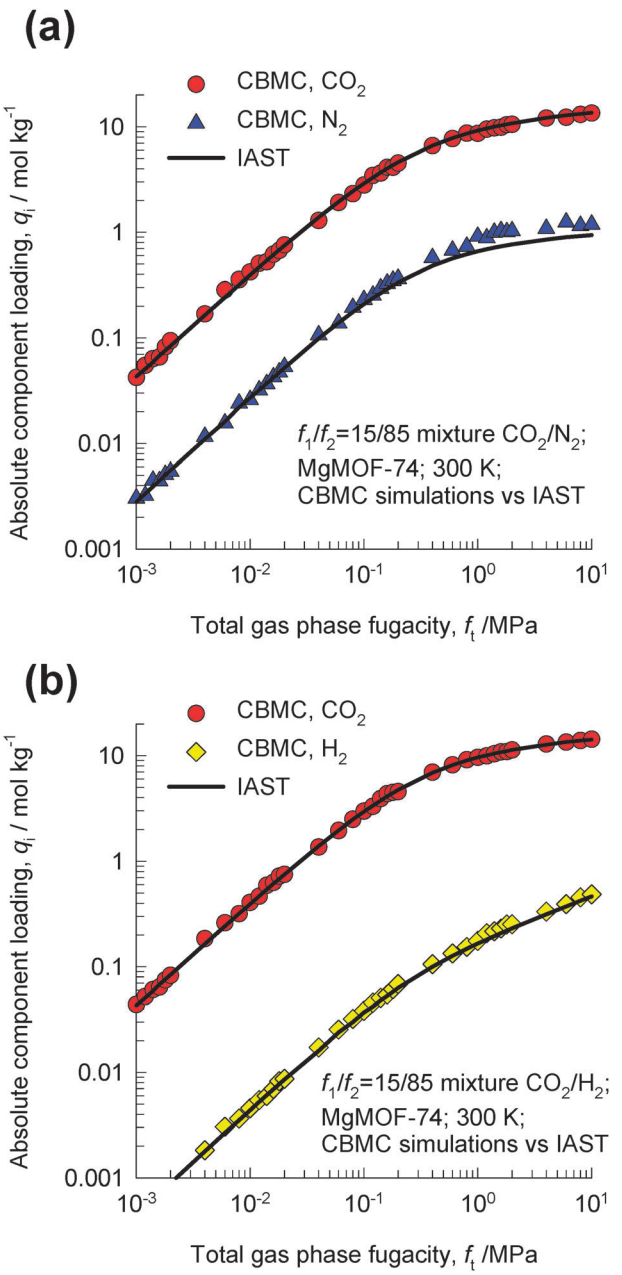

Fig. 8 CBMC simulations for component loadings in (a) CO_2/N_2, and (b) CO_2/H_2 mixtures at 300 K with partial fugacities $f_1/f_2 = 15/85$. The continuous solid lines are the IAST calculations using the dual-Langmuir–Freundlich fits of the CBMC simulated pure component isotherms.

For separation of 20/80 CO_2/H_2 mixtures, the procedure suggested above has been used by Herm *et al.*[29] to compare the values of S_{ads} and Δq of five different MOFs: MgMOF-74, MOF-177, CuBTTri, BeBTB, and Co(BDP), with traditionally used adsorbents such as NaX. Their study concludes that while the S_{ads} value of MgMOF-74 is higher than that of NaX and has the additional advantage of having a significantly higher Δq. Their conclusions are entirely in line with those that can be deduced from molecular simulations and presented Fig. 6c. It is also instructive to compare the IAST calculations of S_{ads} and Δq published by Herm *et al.*[29] with corresponding CBMC mixture simulations; the two sets are compared in Fig. 9. We observe reasonable agreement between these two sets; this lends credence to the use of the screening procedure used in this paper. Another point to note is that the CBMC simulations of S_{ads} value of MgMOF-74 are lower than that found by Herm *et al.*[29] The most likely reason for this is that the force fields used for MgMOF-74 do not take account of orbital interactions,[28] as has already been stressed in a foregoing paragraph.

The breakthrough characteristics of a packed bed adsorber are determined by both the metrics: S_{ads} and Δq; for a specific adsorbent the breakthrough times can be calculated from transient adsorber simulations, along with the IAST equilibrium model.[61]

4. Screening of MOF and zeolite membranes for CO_2 capture

For screening of MOF and zeolite membranes, we need to additionally consider the diffusivities of guest molecules within the pores. The $D_{i,self}$ values vary by several orders of magnitude depending on the pore size and connectivity; they are also dependent on the loading or concentration within the pores. For illustration purposes, Fig. 10a presents MD simulated $D_{i,self}$ data for pure CO_2 in a variety of microporous structures as a function of the concentration. The concentrations c_i plotted on the x-axis in Fig. 10a are expressed as the number of moles per m^3 of accessible pore volume, $c_i = q_i/V_p$. This concentration measure allows a proper comparison of the loadings in structures having widely different pore volumes; further detailed discussions on the merits of this concentration measure are available in the literature.[15,63,66] The $D_{i,self}$ values decrease as the pore concentrations c_i approach the saturation concentrations, $c_{i,sat}$, that has a value $\sim$30 kmol m^{-3}, corresponding to the liquid phase density of CO_2 within the pores at 300 K. CBMC simulations of the pure component isotherm data, presented in Fig. 10b, confirm that $c_{i,sat} \approx$ 30 kmol m^{-3} for all microporous structures. The $D_{i,self}$ *vs.* c_i data can display a maximum when (1) molecular clustering occurs,[52,131,133,138,139] or (2) when the guest molecules have to jump across narrow windows separating adjacent cages.[126,127]

Broadly speaking the hierarchy of diffusivity values in Fig. 10a is dictated by two factors: (1) the characteristic pore

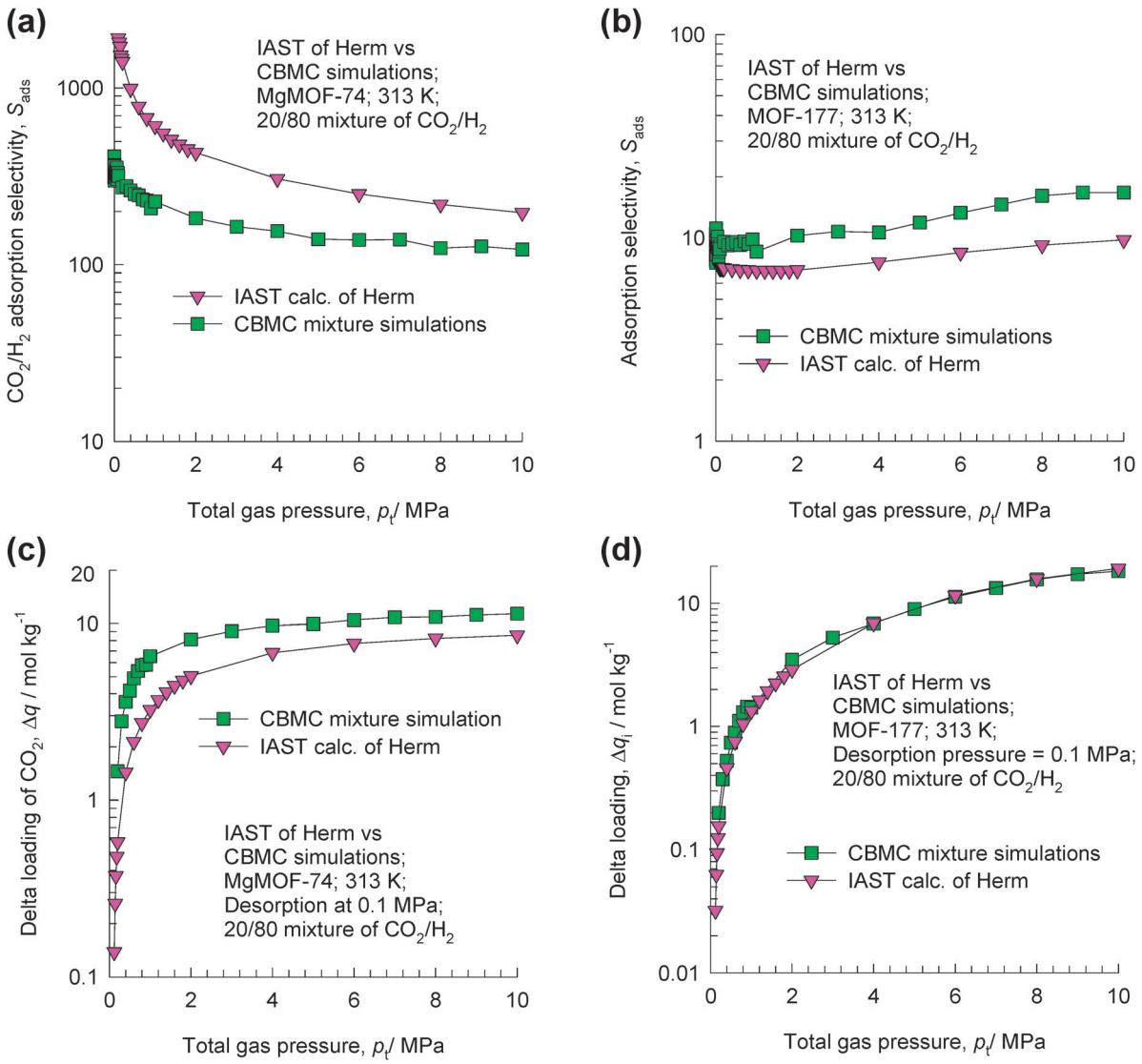

Fig. 9 (a) Adsorption selectivity, S_{ads}, and (b) delta loadings, Δq, for 20/80 CO_2/H_2 mixture separation with MgMOF-74 at 313 K. Comparison of the IAST calculations of Herm *et al.*[29] using their pure component isotherm fits, with CBMC mixture simulations.

dimensions and (2) the binding energy of CO_2. Fig. 10c presents the molecular simulation data on the isosteric heats of adsorption of CO_2 within a variety of structures; these data give a good reflection of the hierarchy of the binding energies. Consider the three structures FAU–Si, NaY (54 Na^+ per unit cell), and NaX (86 Na^+ per unit cell) that have the same pore topology with a pore dimension (window aperture) of 7.4 Å, but with increasing number of cations. Increasing the number of cations increases the binding energy of CO_2, due to increased electrostatic interactions. From Fig. 10c we note that the heats of adsorption follow the hierarchy NaX > NaY > FAU–Si, and this explains why the $D_{i,self}$ values for CO_2 have the inverse hierarchy FAU–Si > NaY > NaX. A higher sticking tendency implies a lower mobility.[63] Fig. 10c shows that the heat of adsorption of CO_2 in MgMOF-74 is significantly higher than for ZnMOF-74; the stronger binding energy with Mg atoms accounts for the significantly lower diffusivity of CO_2 in MgMOF-74 when compared to ZnMOF-74, despite the fact that the channel dimensions of these two MOFs are the same, both being 11 Å. Consider the two structures CHA and ZnMOF-74; these have nearly the same heats of adsorption. The diffusivity of CO_2 in CHA, with a window aperture of 3.77 Å × 4.23 Å, is about an order of magnitude lower than that for ZnMOF-74 (with 11 Å channels) because of the much stronger constriction at the window regions. The highest diffusivity is obtained in MOF-177 that has the lowest heat of adsorption. A further demonstration of the influence of the binding energy is to consider the diffusivity, in the limit of low pore concentrations, of a variety of guest molecules in the same host structure: MgMOF-74; see Fig. 10d. The zero-loading diffusivity decreases with increasing heat of adsorption.[140] The inescapable conclusion that is to be drawn from the foregoing discussions is that, generally speaking, adsorption and diffusion do not go hand in hand. A stronger adsorption strength implies a lower membrane permeability.

Let us turn our attention to the diffusion selectivity, S_{diff}, defined by eqn (5). MD simulation results for S_{diff} for

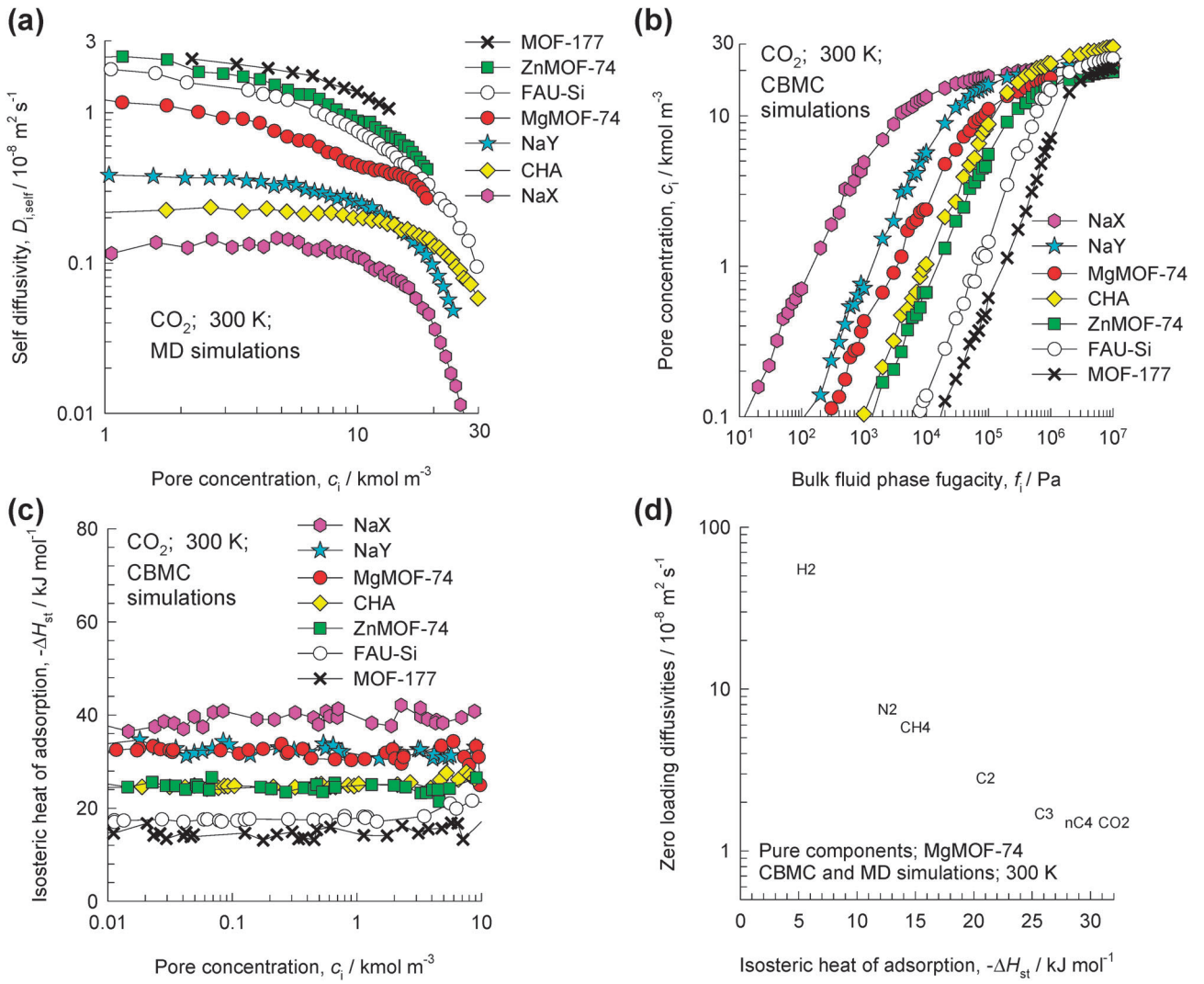

Fig. 10 (a) Self-diffusivity $D_{i,self}$ from MD simulations for pure CO_2 in a variety of microporous materials as a function of the pore concentration c_i. (b) CBMC simulation data for isotherms of CO_2 in a variety of microporous materials. (c) CBMC simulations of the isosteric heats of adsorption of CO_2 in a variety of microporous materials. (d) Dependence on the isosteric heat of adsorption of the zero-loading diffusivities of a variety of guest molecules (H_2, N_2, CH_4, ethane, propane, *n*-butane, and CO_2) in MgMOF-74 at 300 K.[140]

equimolar (*i.e.* $c_1 = c_2$) CO_2/H_2 mixtures are presented in Fig. 11a for a few typical MOFs and zeolites. Due to the much smaller molecular size of H_2 molecules, the S_{diff} in all microporous structures is lower than unity. In all structures, the S_{diff} is lower than the Knudsen selectivity value $\sqrt{M_2/M_1} = 0.213$ at low pore concentrations; this is because the classical Knudsen prescription only holds when the species have negligible adsorption at the pore walls.[52,63,141–143] The hierarchy of S_{diff} is the same as the hierarchy for the self-diffusivities of pure CO_2, presented in Fig. 10a. For the same FAU topology we find the S_{diff} values for FAU, NaY, and NaX to be 0.24, 0.055, and 0.018 for a pore concentration of 10 kmol m^{-3}, a hierarchy that is opposite to the S_{ads} data presented in Fig. 3c. Increasing adsorption strength by enhancing the electrostatic interactions of CO_2 with Na^+ has the effect of reducing the mobility of CO_2 relative to that of H_2; these results are in line with those presented in Fig. 10a, and can be attributed to increased sticking tendency.[63,142] As is to be expected, the S_{diff} for MgMOF-74 is lower than that for ZnMOF-74; this hierarchy is opposite of the hierarchy in S_{ads} data presented in Fig. 3c. For membrane permeation this essentially implies that S_{diff} counteracts the gain in S_{ads}. Another noteworthy point is that the S_{diff} values increase with increasing pore concentrations, c_t; these values can also exceed the Knudsen selectivity. This is because the molecular motions get increasingly *correlated* as the total concentration of guest molecules increases.[15,63–65,144] At pore saturation conditions, when correlation effects are dominant the diffusion selectivities can reach unity values.[144] Correlated motion of molecules has the effect of slowing down the more mobile H_2, and increasing S_{diff}. Video animations of the motion of CO_2/H_2 and CH_4/H_2 mixtures in MgMOF-74 give some visual, albeit qualitative, appreciation of the slowing-down of H_2 molecules by the partner species; these animations are available as ESI.† Since the slowing-down effects manifest in mixtures, the value of S_{diff} cannot be calculated using *pure* component diffusivity

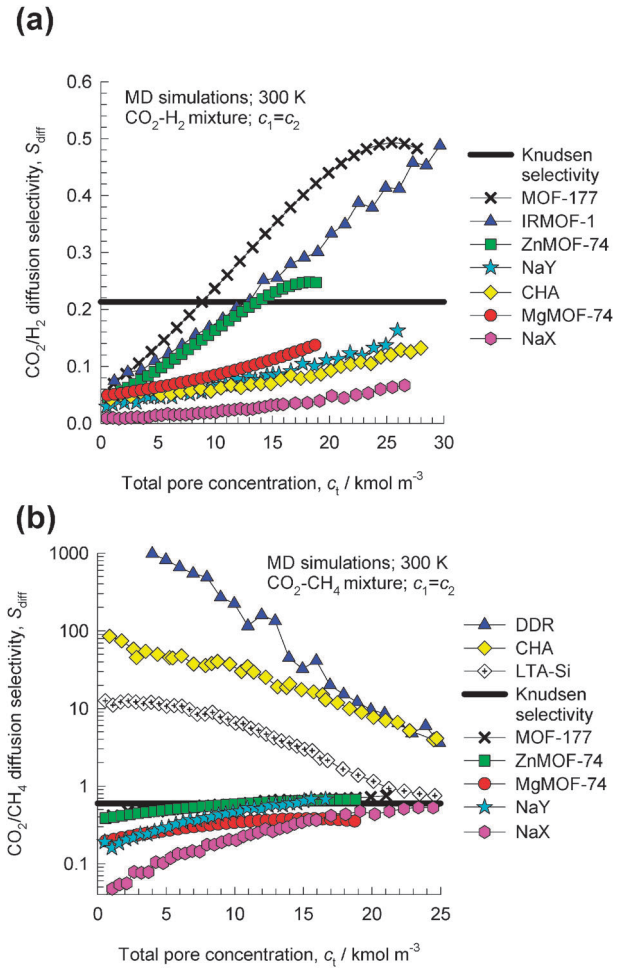

Fig. 11 Diffusion selectivities, S_{diff}, for equimolar ($c_1 = c_2$) (a) CO_2/H_2, and (b) CO_2/CH_4 mixtures at 300 K, plotted as a function of the total pore concentration $c_t = c_1 + c_2$.

data; there are, however, exceptional cases and these are discussed later in this article.

Let us now analyze the diffusional selectivities for CO_2/CH_4 mixtures, for which the Knudsen selectivity value is 0.6. In 1D channels, intersecting channels, and open structures for which the pore sizes are larger than about 5.5 Å, the MD simulated value of S_{diff} is lower than 0.6; see Fig. 11b. This is mainly due to the fact that the higher adsorption strength of CO_2 lowers its mobility within the micropores. In the limit of low pore concentrations, the S_{diff} of CO_2/CH_4 mixtures in MgMOF-74 is found to be 0.2; this value is in excellent agreement with the value obtained in the experiments of Bao *et al.*[18]

CO_2 is a more slender molecule than CH_4 and a different scenario holds for zeolites with 8-ring windows, such as ERI, CHA, ITQ-29, DDR, TSC, and LTA. For these structures, the S_{diff} is significantly higher than unity. CH_4 is highly constrained at the windows of 3.4 Å–4.1 Å dimensions and has a significantly lower diffusivity. Fig. 12 presents a snapshot showing the location of CO_2 and molecules in LTA zeolite; it can be seen that CO_2 perches length-wise at the windows. Video animation of CO_2/CH_4 mixture diffusion in LTA, that is available as ESI†, demonstrates the length-wise hop of CO_2 from one cage to the next. Furthermore, the preferential

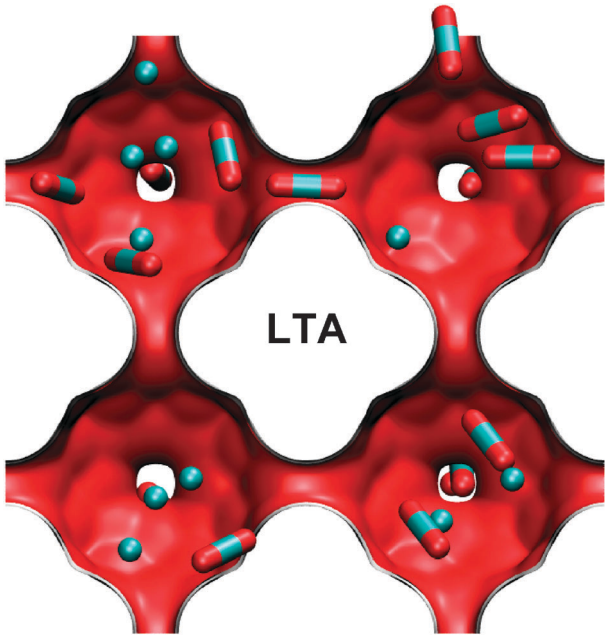

Fig. 12 Snapshot showing the location of CO_2 and CH_4 molecules in LTA zeolite.

location of CO_2 at the window regions of LTA and DDR serves to hinder the inter-cage hopping of CH_4; this explains why $S_{diff} \gg 1$.[130,132] The hierarchy of S_{diff} in Fig. 11b is dictated, broadly speaking, by the hierarchy of window sizes; the smaller the window size, the higher is the value of S_{diff}.[126,127]

To illustrate the importance of correlation effects, Fig. 13 presents MD data on the diffusion selectivities of binary CO_2/CH_4, CO_2/N_2, and CO_2/H_2 mixtures in MgMOF-74 as a function of the mole fraction of CO_2 in the adsorbed phase.

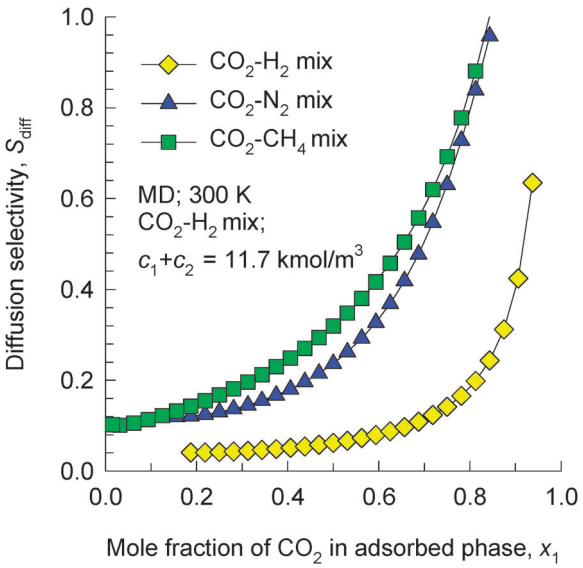

Fig. 13 Diffusion selectivities of binary CO_2/CH_4, CO_2/N_2, and CO_2/H_2 mixtures in MgMOF-74 at 300 K as a function of the mole fraction of CO_2 in the adsorbed phase. The total mixture loading is kept constant at a value of 20 molecules per unit cell, corresponding to $c_t = 11.7$ kmol m^{-3}.

The total pore concentration c_t is kept constant at a value of 11.7 kmol m^{-3} for all three mixtures. Increasing the proportion of the tardier species CO_2 reduces the diffusivities of the three, more mobile, partner species and as the proportion of CO_2 in the adsorbed phase increases, the diffusion selectivities approach unity values. Correlation effects are particularly strong in 1D channels. On the other hand for structures such as LTA, CHA, DDR, ERI, and ZIF-8, that have cages separated by narrow windows in the 3.4 Å–4.1 Å range, correlation effects are considerably weaker because only one molecule at a time can jump between cages. When correlations are weak, the S_{diff} can be estimated using pure component diffusivity data.[63–65]

The experimental data presented by Bux *et al.*[59] for CO_2/CH_4 mixture diffusion in ZIF-8 yields an S_{diff} value of the order of unity, despite the fact that the window size of this structure is 3.4 Å, smaller than that of DDR which displays a S_{diff} value about 2–3 orders of magnitude higher.[127] This would suggest that the dynamics of the window opening of ZIF-8 are different to those of 8-ring zeolites.[126,127] In this context it is noteworthy that Gücüyener *et al.*[46] have postulated a gate-opening mechanism to explain the permeation of ethane/ethene mixture across a ZIF-7 membrane. A qualitative appreciation of the gate-opening mechanism can be obtained from the video animation of the framework dynamics of ZIF-8 that is available as ESI.† The paper by Bux *et al.*[59] also provides experimental confirmation of the accuracy of CBMC simulations to estimate the S_{ads} of CO_2/CH_4 mixtures in ZIF-8.

Fig. 14 presents data on the permeation selectivities, S_{perm}, calculated by multiplying the adsorption selectivity values S_{ads} with the S_{diff} value, determined at a total pore concentration $c_t = c_1 + c_2$ at the upstream membrane face, in equilibrium with the gas mixture at the total fugacity value f_t. The S_{perm} values reflect the balance between adsorption and diffusion for the four different mixtures in different structures. Broadly speaking, S_{ads} and S_{diff} do not complement each other. For permeation of CO_2/CH_4, CO_2/N_2, and CO_2/H_2 mixtures across MgMOF-74 and ZnMOF-74 membranes, we note that S_{perm} is higher for MgMOF-74 despite having a lower S_{diff} value. This indicates that the higher S_{ads} for MgMOF-74 more than compensates for the lower S_{diff}. For CH_4/H_2 mixture permeation both MgMOF-74 and ZnMOF-74 exhibit similar S_{perm} values.

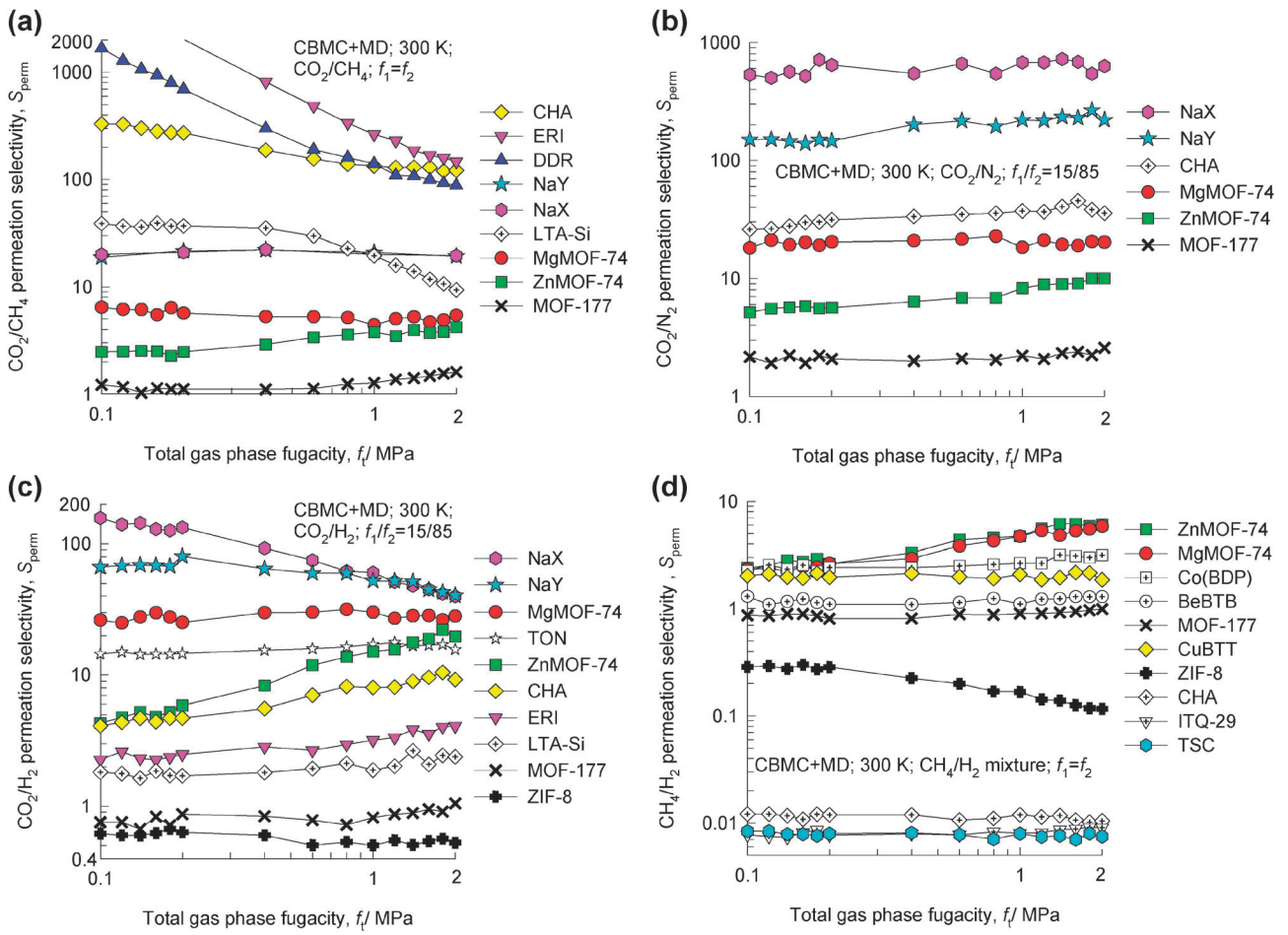

Fig. 14 Permeation selectivities, S_{perm}, for (a) CO_2/CH_4, (b) CO_2/N_2, (c) CO_2/H_2, and (d) CH_4/H_2 mixture permeation at 300 K across a variety of MOFs and zeolite membranes. In (a) and (d) the partial fugacities in the gas phase in the upstream compartment are equal, *i.e.* $f_1 = f_2$. In (b) and (c) the gas phase partial fugacities satisfy $f_1/f_2 = 15/85$. For clarity of presentation only a selection of the simulation data is presented here; the complete set of data are available in the ESI.†

Let us now consider the effect of extra-framework cations on membrane permeation. For CO_2/CH_4 and CO_2/H_2 mixture permeations across NaX and NaY membranes nearly the same values of S_{perm} are obtained, despite the fact that NaX has a significantly higher S_{ads}. This would suggest that increasing electrostatic interactions by introducing more extra-framework cations, beyond a certain value, could become counter-productive. The highest permeation selectivities for CO_2/CH_4 separation are obtained with zeolites with 8-ring windows such as DDR, CHA, and ERI. In all these cases S_{ads} and S_{diff} complement each other; this is a rather unique situation.

Besides S_{perm}, the cost of membrane separations is dictated by the permeability, Π_i. For a specified feed throughput the permeability value dictates the total membrane surface area that is required. For all four mixtures, the permeability was determined using the self-diffusivity value of that component from MD mixture simulations, calculated at the total pore concentration corresponding to conditions at the upstream membrane face. For an arbitrarily chosen upstream value of f_t = 1 MPa, the values of S_{perm} are plotted against the corresponding Π_i value in Fig. 15 for the four different mixtures. These plots are essentially equivalent to the conventionally used Robeson plots for polymeric membranes.[15,145] These can be also be considered as analogs of the S_{ads} *vs.* Δq plots in Fig. 6. The straight lines in Fig. 15a and b represent the "Robeson upper bound" values that are obtainable with polymer membranes. The ideal choice of the microporous structure would correspond to conditions at the top right hand corner of the diagram. For the reasons discussed in the foregoing paragraphs, high values of S_{perm} rarely go hand in hand with high Π_i.

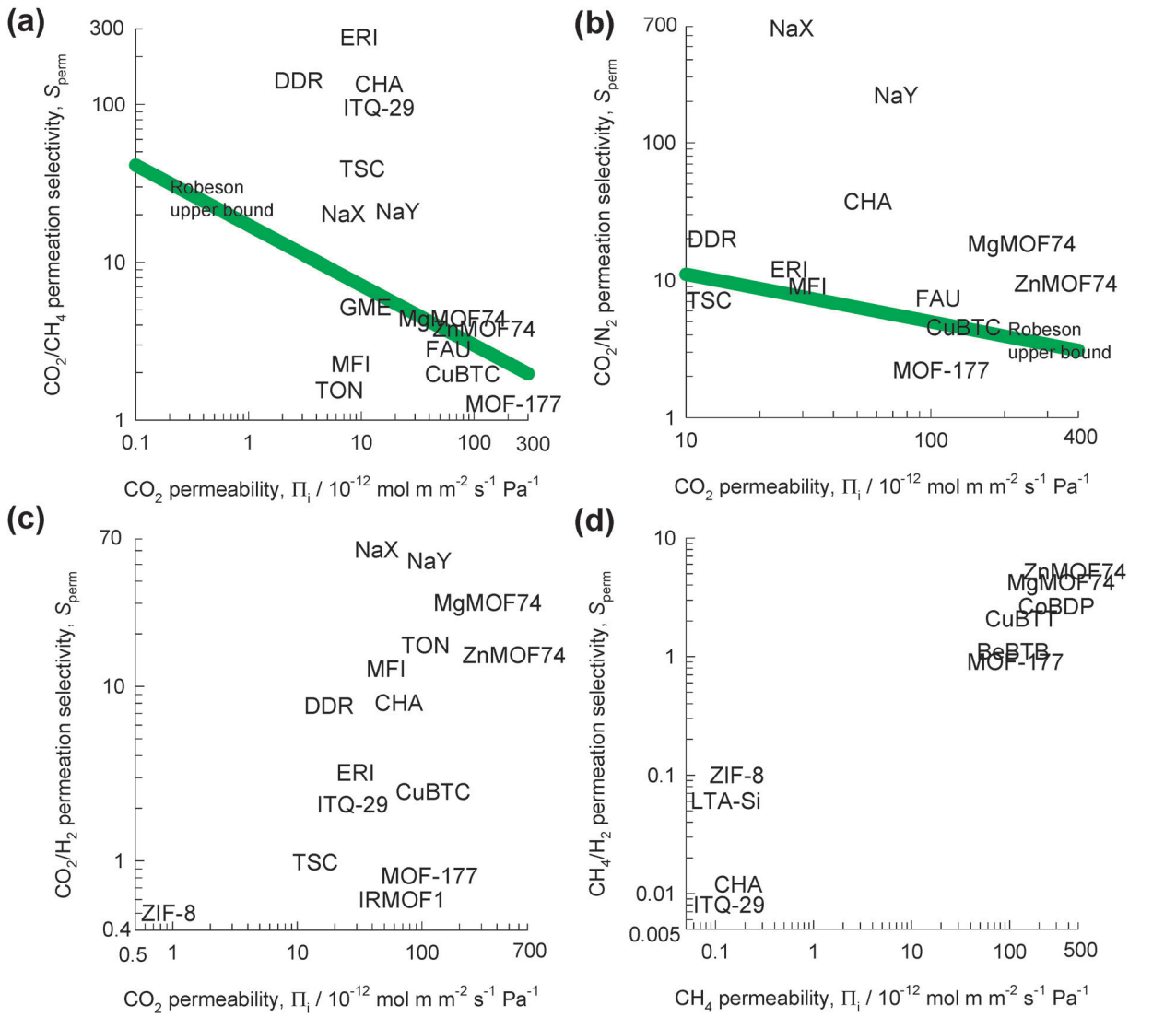

Fig. 15 Robeson plots in which permeation selectivities, S_{perm}, for different microporous structures plotted against the permeability, Π_i, for (a) CO_2/CH_4 (b) CO_2/N_2, (c) CO_2/H_2, and (d) CH_4/H_2 mixture permeation at 300 K across a variety of MOFs and zeolite membranes. The chosen conditions correspond to a total bulk gas phase fugacity f_t = 1 MPa. The downstream conditions are chosen to be such that $f_t \approx 0$ MPa. For clarity of presentation only a selection of the simulation data is presented here; the complete set of data are available in ESI.† In (a) and (b) "upper bound" values for polymeric membranes are calculated using the parameters specified in Table 12 of Robeson.[145]

For CO_2/CH_4 mixture separation, values of $S_{perm} > 100$ are obtained with ERI, DDR, and CHA. For DDR and CHA, there is experimental evidence that such high permeation selectivities can be realized in practice.[130,146–151] For CO_2/N_2 separation, S_{perm} values exceeding 200 are obtained with NaX and NaY zeolites; there is experimental evidence that the predicted permeation selectivities for NaY can indeed be realized.[152–155] More detailed modelling studies of CO_2/H_2 and CO_2/N_2 permeation across MgMOF-74 membranes indicate that the S_{perm} results presented in Fig. 15 are too conservative, and significantly higher permeation selectivities can be obtained when upstream pressures exceed 1 MPa.[140] The reason for this is that the correlation effects are significantly enhanced within the 1D channels when there is a preponderance of CO_2 molecules as is evidenced by the data presented in Fig. 13.

For CH_4/H_2 mixture permeation, the data in Fig. 15d suggest that MgMOF-74 is the "optimum" MOF structure that offers the best combination of S_{perm} and Π_i values. In the computational screening study of Keskin[42] it was concluded that the best MOF for this task is CoMOF-74 that has similar adsorption and diffusion characteristics as MgMOF-74.

For CO_2/H_2 mixtures, use of ZIF-8, a structural analog of SOD zeolite, is seen to yield $S_{perm} < 1$, indicating H_2-selective permeation. There is recent experimental evidence in the literature to confirm that such a H_2-selective separation is possible with ZIF-7, that has a structure similar to that of ZIF-8.[41] For CH_4/H_2 mixtures, structures such as ZIF-8, LTA–Si, ITQ-29, and CHA, that have narrow windows separating cages, allow H_2-selective permeation; there is confirmatory experimental evidence in the published literature.[40,151,156]

5. Screening of MOFs and zeolites for separation of hydrocarbon mixtures

Isomerization of alkanes, for the purposes of octane improvement, is a process of importance in the petroleum industry.[157–159] Fig. 16a shows an example of a process for isomerization of *n*-hexane (*n*C6). The product from the isomerization reactor, that commonly uses zeolite MOR as a catalyst, consists of an equilibrium distribution of unreacted *n*C6, along with its mono-branched isomers 2-methylpentane (2MP), 3-methylpentane (3MP) and di-branched isomers 2,2-dimethylbutane (22DMB) and 2,3-dimethylbutane (23DMB). In current industrial practice the linear *n*C6 is separated from the branched isomers in an adsorption separation step that relies on molecular sieving. The adsorbent is LTA-5A that consists of cages separated by 4.1 Å sized windows. The windows only allow the diffusion, and adsorption of the linear isomer, and the branched isomers are rejected and removed as a product. The unreacted *n*C6 is recycled back to the isomerization reactor.

The values of the Research Octane Number (RON) increase with the degree of branching: *n*C6 = 30, 2MP = 74.5, 3MP = 75.5, 22DMB = 94, 23DMB = 105.[100,160] Therefore di-branched isomers are preferred products in an isomerization process. An improved process would require the recycle of both linear and mono-branched isomers to the reactor; see Fig. 16b. The separation of 22DMB and 23DMB from the

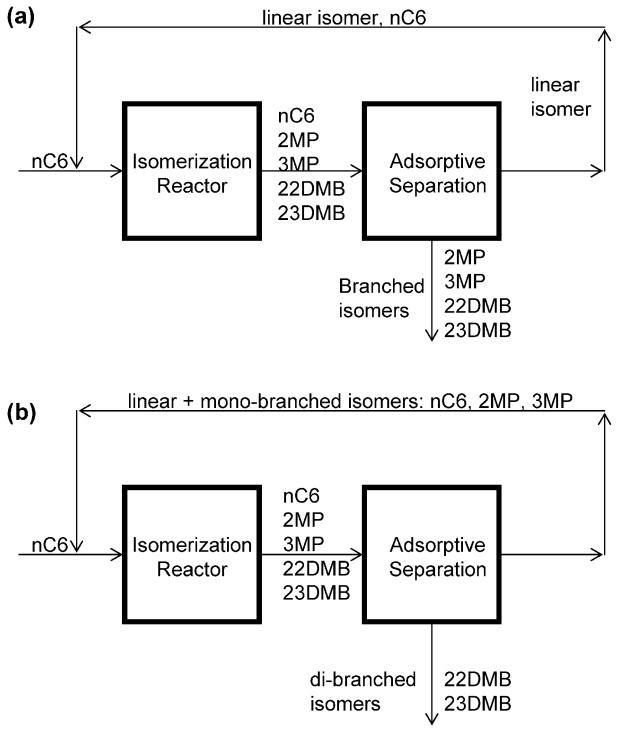

Fig. 16 (a) Conventional process flow scheme for alkane isomerization. (b) Suggested improved process for alkane isomerization.

remaining isomers is a difficult task because it requires distinguishing molecules on the *degree* of branching. There are indications from the patent literature that this separation can be achieved using a zeolite adsorbent, and a wide variety of zeolites are mentioned as candidate adsorbents.[158,159] In screening studies of separation of hexane isomers using zeolites, it was concluded that highest selectivities in favour of the linear *n*C6, and decreasing with the degree of branching, are obtained in MFI.[73,100,161,162] The use of PSA units for hexane isomer separations using MFI adsorbents has been demonstrated.[67,160,163–165] With the wide variety of MOFs currently on offer, it is interesting to investigate whether MOFs can be effective for hexane isomer separation. Bárcia *et al.*[92] performed breakthrough experiments for *n*C6/3MP/22DMB mixtures and have reported the separation hierarchy *n*C6 ≫ 3MP ≈ 22DMB, which is not the desired one in the process scheme of Fig. 16b. In a more recent study Bárcia *et al.*[166] found that the MOF UiO-66 preferentially adsorbs the dibranched 22DMB and 23DMB molecules.

Before we consider the separation of 5-component *n*C6/2MP/3MP/22DMB/23DMB mixtures, we shall elucidate the underlying principles by carrying out CBMC mixture simulations for adsorption of an equimolar ($f_1 = f_2 = f_3$) ternary *n*C6/3MP/22DMB mixture in a variety of MOFs: MgMOF-74, ZnMOF-74, CuBTT, Co(BDP), BeBTB, MOF-177, and IRMOF-1. For comparison purposes we also carried out simulations with a variety of zeolites (MFI, AFI, BEA, FAU–Si, LTA–Si, LTL, NaY, NaX).

Four typical mixture adsorption characteristics, displayed by MFI, AFI, Co(BDP), and MgMOF-74, are depicted in Fig. 17, which presents CBMC simulation data on the component loadings in the adsorbed phase in equilibrium with

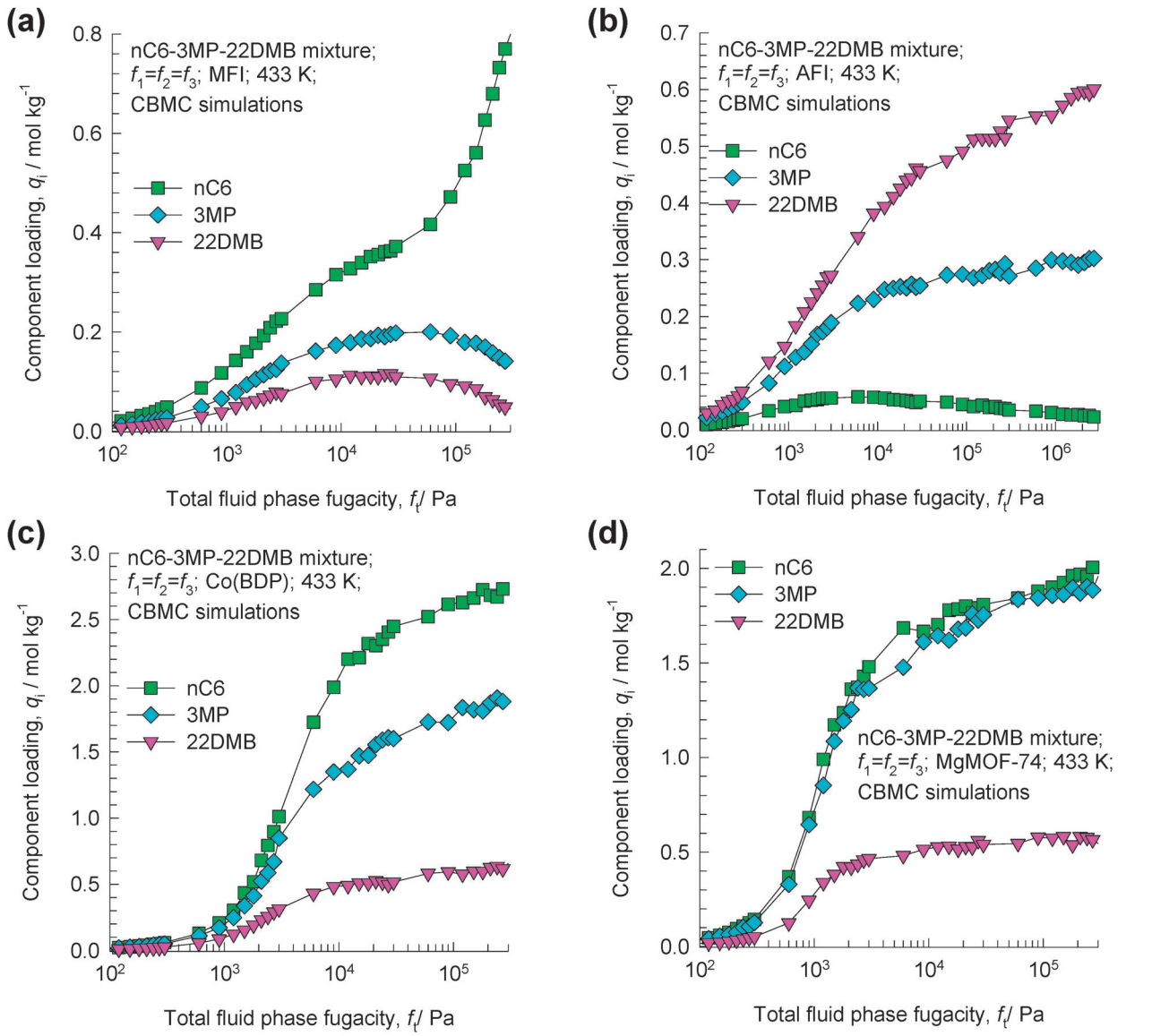

Fig. 17 CBMC simulations of adsorbed phase loadings in equilibrium with equimolar ($f_1 = f_2 = f_3$) ternary *n*C6–2MP–22DMB mixtures in (a) MFI, (b) AFI, (c) Co(BDP), and (d) MgMOF-74 at 433 K.

equimolar ternary gas phase containing *n*C6–3MP–22DMB mixtures. For MFI, the adsorption hierarchy is *n*C6 > 3MP > 22DMB; see Fig. 17a. This is dictated by the fact that the *n*C6 can locate along either the straight or zig–zag channels, whereas 22DMB can locate only at the channel intersections that offer additional "leg room"; see snapshot in Fig. 18a. 3MP also prefers to locate at the intersections, and can be located within the channels only at very high pressures.

The reverse hierarchy *n*C6 < 3MP < 22DMB is obtained for adsorption within the 0.73 nm sized one-dimensional channels of AFI; see Fig. 17b. This hierarchy can be rationalized by examining the snapshot in Fig. 18b of the molecular configurations within AFI. The linear *n*C6 has a longer "footprint" and occupies a larger segment of the channel. 22DMB is the most compact molecule and has the smallest footprint; consequently, more molecules of 22DMB can be located within a given length of AFI channels when compared to *n*C6. 3MP has a footprint that is intermediate in character. *Molecular length entropy* effects dictate the sorption hierarchy in AFI, and a similar situation holds for MOR that has 0.65 nm × 0.7 nm sized 1D channels.[100,167] The experiments of Bárcia *et al.*[166] with UiO-66 suggests that molecular length entropy effects dictate the observed adsorption hierarchies.

For all the MOFs investigated here, the adsorption hierarchy is either *n*C6 > 3MP > 22DMB or *n*C6 ≈ 3MP > 22DMB; see the CBMC data on component loadings of hexane isomers in Co(BDP) and MgMOF-74 in Fig. 17c and d. In order to rationalize the results let us examine the conformations of hexane isomers within the 1D square-shaped channels of Co(BDP) with an effective diameter of 1 nm in Fig. 19. The linear *n*C6 molecule can wrap itself around the 1D channels in such a manner that each of the six C atoms can interact with the framework. In contrast, the conformation of di-branched 22DMB is such that some of the C atoms must point inward to the centre of the channels; these C atoms can, at best, interact with C atoms of neighboring 22DMB

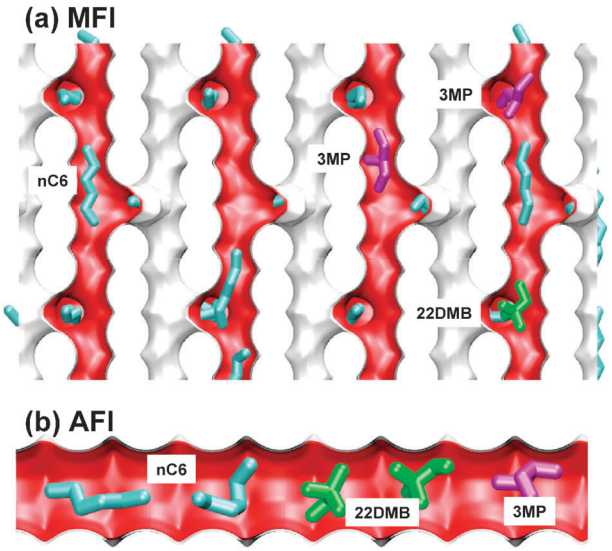

Fig. 18 Snapshots showing the location of *n*C6, 3MP, and 22DMB within (a) the intersecting channels of MFI, and (b) one dimensional channels of AFI.

molecules and are unable to interact with framework atoms. The situation with respect to 3MP is intermediate to that of *n*C6 and 22DMB; this explains why the component loadings follow the hierarchy *n*C6 > 3MP > 22DMB. The structures CuBTT, BeBTB, MOF-177, and IRMOF-1 possess large cages in the 1.1 nm–1.6 nm size range. The surfaces of the cages are nearly "flat", except for concavities in the vicinity of the metal atoms. The linear *n*C6 can adopt conformations allowing all six C atoms to interact with the flat surfaces; this is much more difficult for the branched 22DMB molecules; a visual appreciation of this can be obtained from Fig. 20 and 21 that show the conformations of the three hexane isomers within the pores of BeBTB and IRMOF-1, respectively.

The selectivities for adsorption of *n*C6 and 3MP, in preference to 22DMB, are plotted against the capacity in Fig. 22a. The best selectivities are obtained with Co(BDP), MgMOF-74, and ZnMOF-74. The obtained selectivities for Co(BDP) are higher than for zeolite MFI, that was selected as the "best" structure in earlier screening studies.[73,100] All zeolites examined have significantly lower capacities than MOFs; the zeolites occupy the left portion of Fig. 22a.

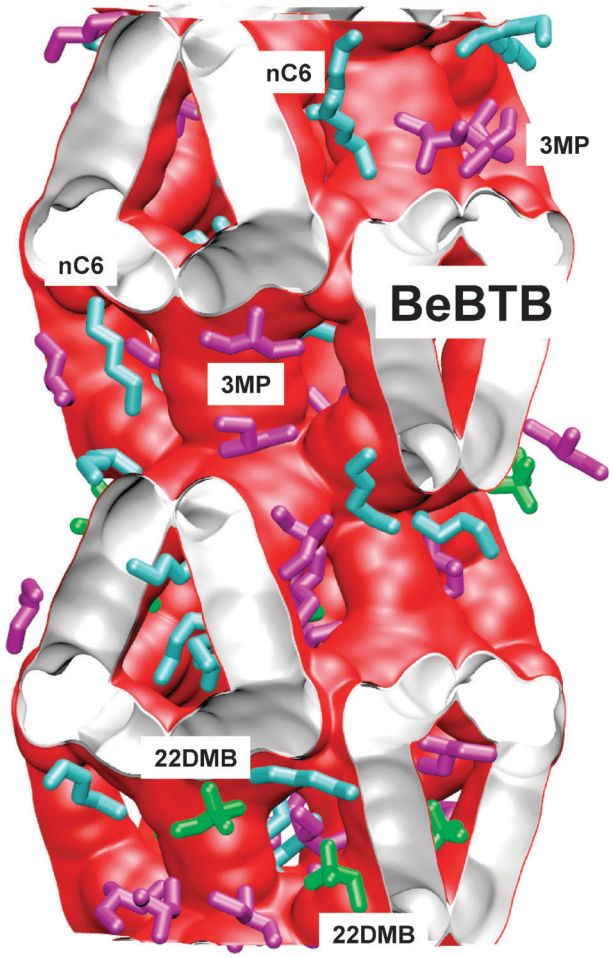

Fig. 20 Snapshot showing the conformations of *n*C6, 3MP, and 22DMB within the pores of BeBTB.

The highest capacities are obtained with MOF-177, BeBTB, IRMOF-1, and Co(BDP) that have highest pore volumes and surface areas. For example, Co(BDP) has a capacity that is about 8 times higher than for MFI.

To obtain further confirmation of the planarity principle of separating alkane isomers, we also carried out simulations for a ternary mixture of pentane isomers: *n*-pentane (*n*C5)–2-methylbutane (2MB)–neopentane (neoP). Analogous

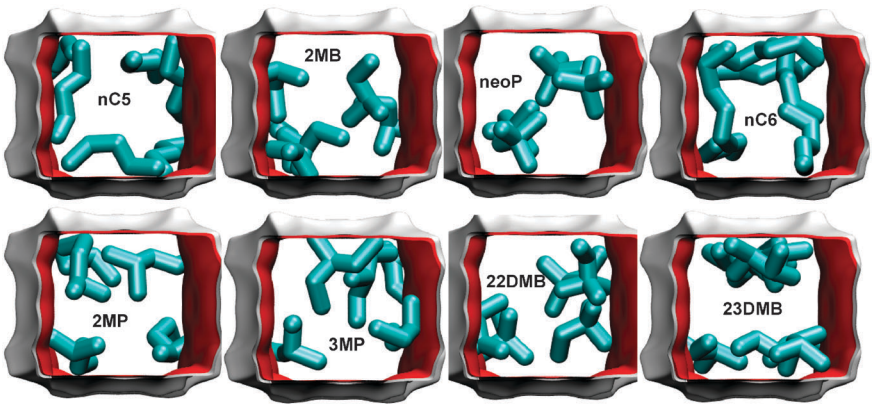

Fig. 19 Snapshots showing the conformations of pentane and hexane isomers within the one-dimensional channels of Co(BDP).

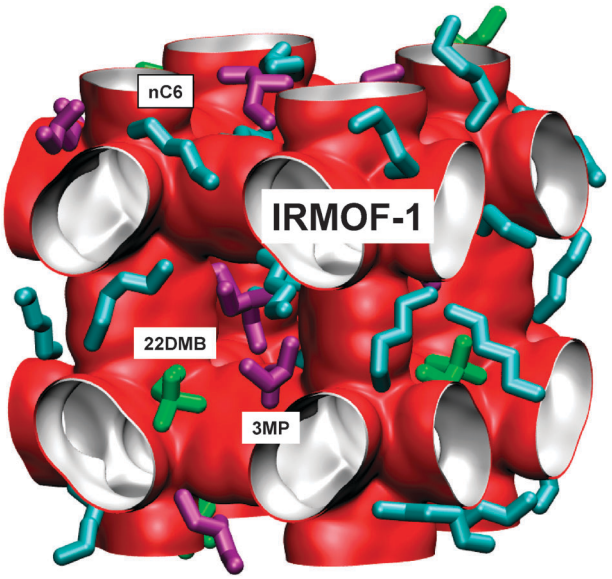

Fig. 21 Snapshot showing the conformations of *n*C6, 3MP, and 22DMB within the pores of IRMOF-1.

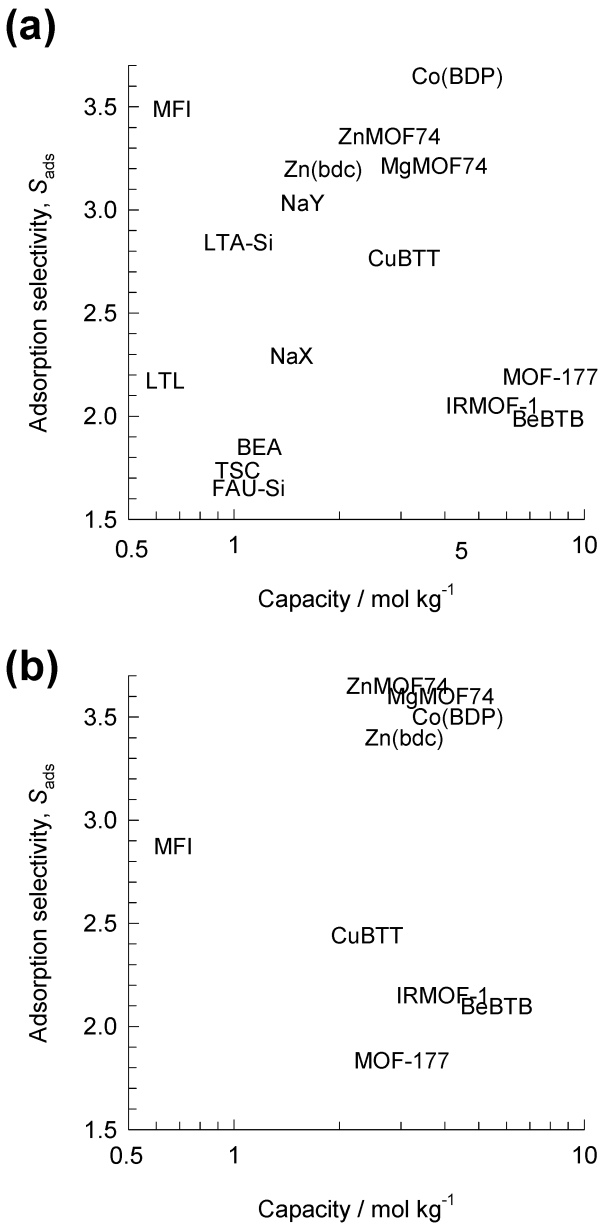

Fig. 22 Adsorption selectivity plotted against the capacity for (a) *n*C6/3MP/22DMB and (b) *n*C5/2MB/neopentane mixtures at 433 K in MOFs and zeolites. The partial fugacities are $f_1 = f_2 = f_3 = 0.03$ MPa. The capacity is the total of the loadings of linear and mono-branched isomers. The adsorption selectivity is defined as the ratio of the combined loadings of linear and mono-branched isomers to that of the di-branched isomer. The data on the component loadings, selectivities, and capacities for all structures are available in the ESI.†

results are obtained; see Fig. 22b. In all cases, the linear and mono-branched isomers have stronger adsorption than the neopentane. The hedgehog-like neopentane molecule cannot adopt conformations that allow optimum van der Waals interactions with the pore walls; see snapshot in Fig. 19. As in the case of hexane isomers, we note that the adsorption selectivities and capacities with Co(BDP), MgMOF-74, and ZnMOF-74 are significantly higher than that for MFI zeolite.

Comparing the molecular conformations of the di-branched hexanes, 22DMB and 23DMB, we note that the latter has a flatter conformation, allowing better van der Waals interaction with the pore walls; see snapshot in Fig. 19. We should therefore expect 23DMB to have stronger adsorption strength than 22DMB. To verify this expectation, we carried out 22DMB/23DMB binary mixture simulations. We found that the 23DMB/22DMB selectivities are greater than unity for all MOFs considered; see detailed information in ESI.† Since 23DMB has a significantly higher adsorption strength in MOFs, it is likely that 23DMB may have the same adsorption strength as the linear and mono-branched isomers. We performed CBMC simulations with the 5-component *n*C6/2MP/3MP/22DMB/23DMB mixture in order to determine whether the hierarchy required in the process flow scheme can be realised. Fig. 23a–d present the data on the component loadings in Co(BDP), MFI, MgMOF-74, and MIL-53(Cr). In the case of Co(BDP) the desired hierarchy *n*C6 > 2MP > 3MP > 23DMB > 22DMB is obtained for the entire range of pressures. Using MFI zeolite (*cf.* Fig. 23b) we need to operate at fugacities $f_t > 0.5$ MPa in order to fulfil the requirements of the process flow scheme in Fig. 16b. Using MgMOF-74, only 22DMB can be separated with high selectivities from the rest of the isomers. The situation with other MOFs (ZnMOF-74, MOF-177, IRMOF-1, BeBTB, Zn(bdc)dabco) is similar to that for MgMOF-74; see ESI† for details. This point is noteworthy because Zn(bdc)dabco has been suggested as a possible candidate for alkane isomer separation in a previous computational study of Dubbeldam *et al.*[54] The situation with respect to MIL-53(Cr), that has 1D channels of 0.74 nm size, is interesting because the obtained hierarchy *n*C6 < 2MP < 22DMB < 3MP < 23DMB would suggest that molecular length entropy effects are in play.

In order to rationalize the results obtained in Fig. 23, we carried out CBMC simulations for graphite slits of widths 0.74 nm, 0.94 nm, 1.14 nm, and 1.34 nm using the methodology that is essentially the same as that of Severson and Snurr;[168]

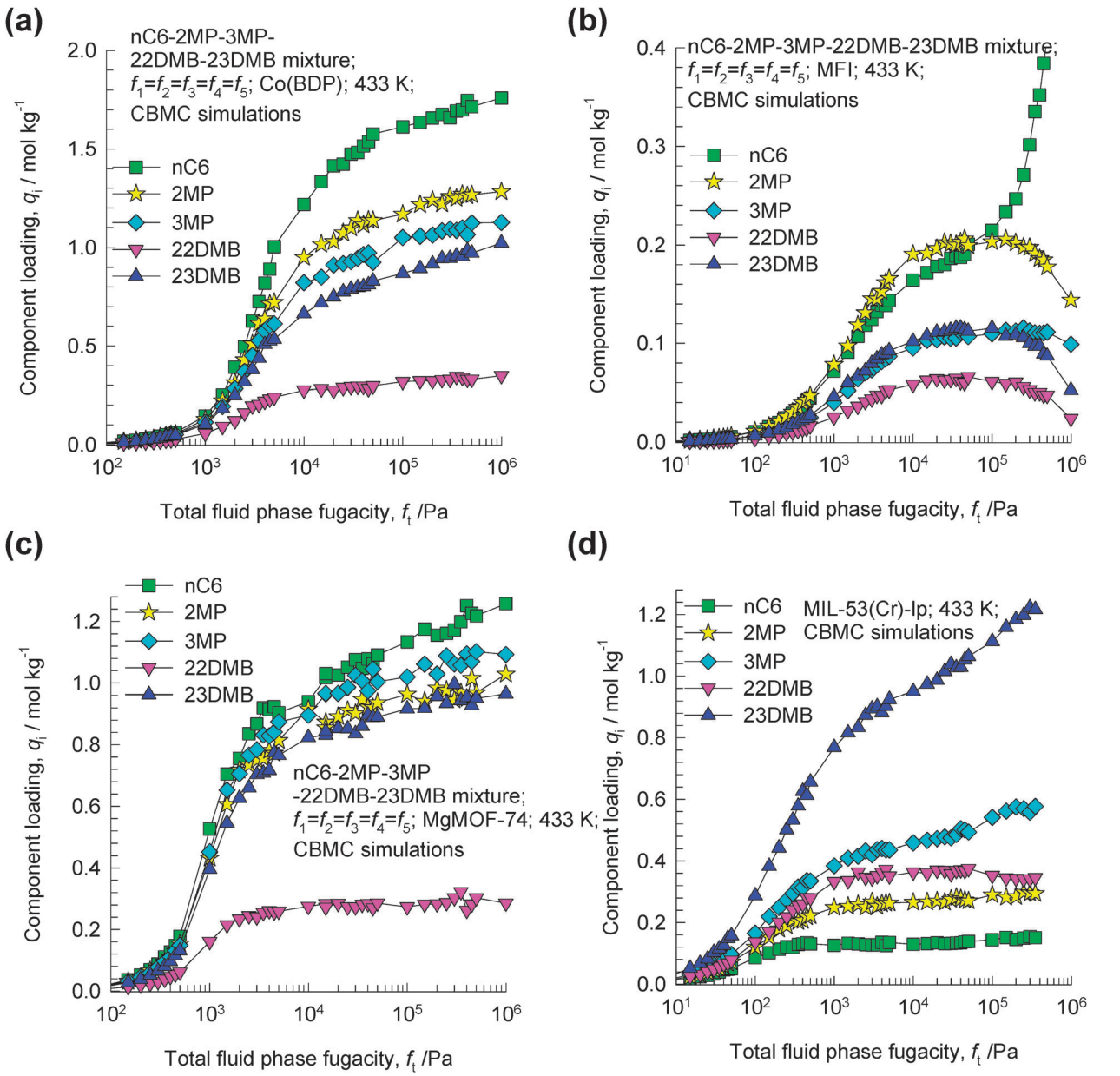

Fig. 23 Component loadings for adsorption of equimolar ($f_1 = f_2 = f_3 = f_4 = f_5$) *n*C6/2MP/3MP/22DMB/23DMB mixtures at 433 K in (a) Co(BDP), (b) MFI, (c) MgMOF-74 and (d) MIL-53(Cr)-lp. Complete data sets for all MOFs are available in the ESI.†

see Fig. 24. The slit width of 0.74 m is small enough to allow all C atoms of each of the guest molecules to have van der Waals interactions with both surfaces on either side of the guest molecules. For the 0.74 nm slit, the obtained hierarchy of 23DMB > 3MP > 2MP > 22DMB > *n*C6 is dictated largely by "footprint" considerations. This hierarchy is precisely the one observed in Fig. 23d for adsorption within the 0.74 nm channels of MIL-53(Cr); this confirms that footprint considerations are important. The hierarchy of adsorption strengths obtained with the 0.94 nm graphite slit is the desired one and corresponds with that obtained with Co(BDP) that has channels that are effectively of 1 nm width. For the 1.14 nm and 1.34 nm graphite slits, the hierarchy of adsorption strengths corresponds with that obtained with MOFs that have channel sizes that are 1.1 nm or larger: MgMOF-74, ZnMOF-74, MOF-177, IRMOF-1, and BeBTB; in these cases only 22DMB can be separated from the other isomers. On the basis of the information presented in Fig. 23, and in the ESI†, we conclude that Co(BDP) is the best structure for hexane isomer separation and experimental confirmation is required in this respect and to establish its superiority over MFI zeolite for use in PSA units.

Consider adsorption of C8 hydrocarbon mixture consisting of *n*-octane (*n*C8), ethyl benzene (EtBz), and *o*-, *m*-, *p*-xylenes within the one-dimensional, diamond-shaped channels of MIL-47. The xylene isomers are "flatter" than *n*C8 and EtBz; they can align themselves parallel to the channel walls (*cf.* snapshots in Fig. 25), affording better van der Waals interactions with the framework atoms. Furthermore, the xylene isomers have a higher "stacking efficiency" within the

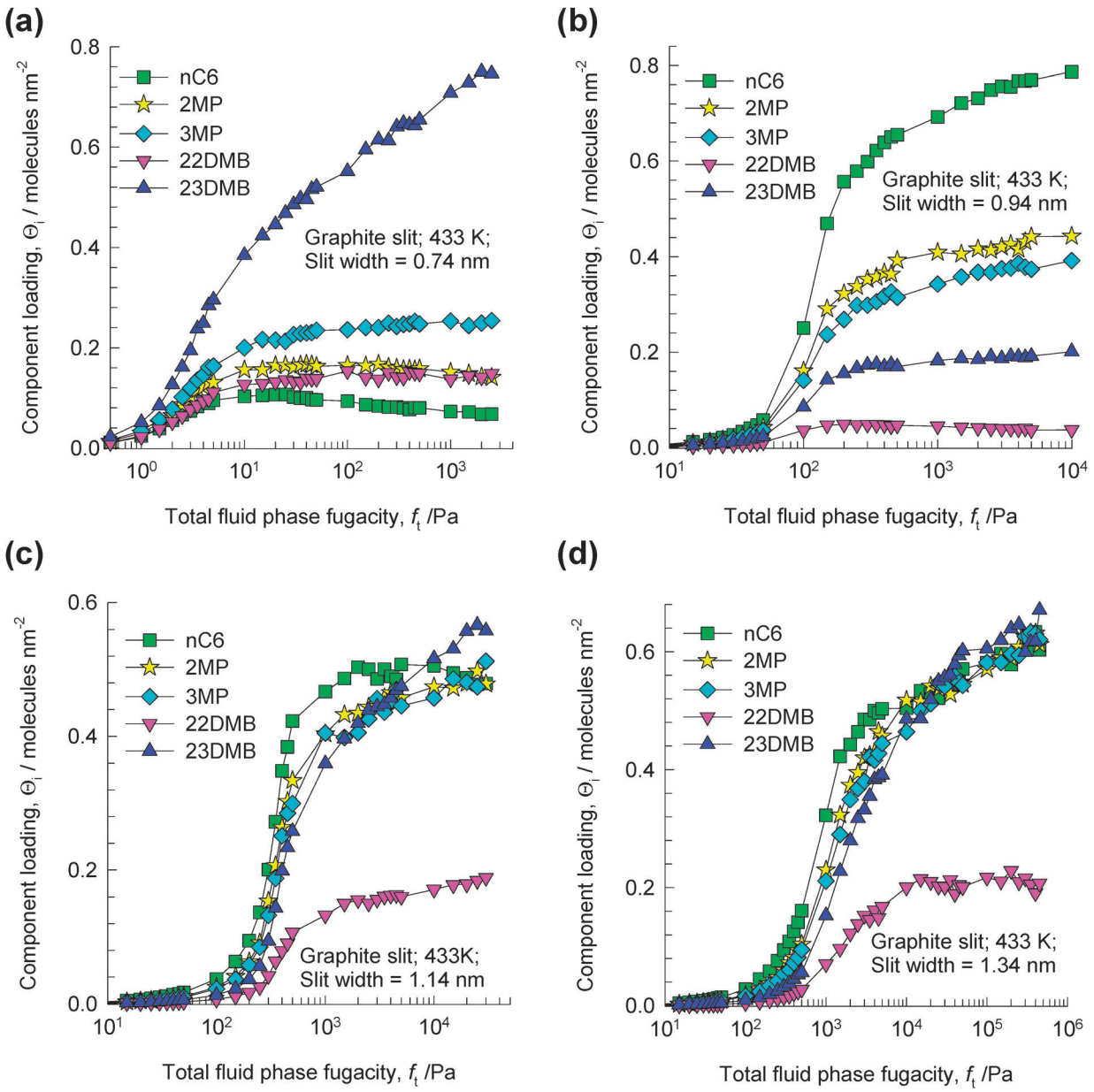

Fig. 24 Component loadings for adsorption of equimolar ($f_1 = f_2 = f_3 = f_4 = f_5$) *n*C6/2MP/3MP/22DMB/23DMB mixtures at 433 K in graphite slits of widths (a) 0.74 nm, (b) 0.94 nm, (c) 1.14 nm, and (d) 1.34 nm. Complete data set for all slits is available in the ESI.† Also available in the ESI† are snapshots showing the conformations of the pure component adsorption on the flat surfaces.

channels. Essentially, MIL-47 offers the appropriate "bookshelf" structure that is required to stack the flat xylene molecules. A higher stacking efficiency implies a higher saturation capacity, and the experimental data of Finsy *et al.*[90] for the pure component isotherms confirm this expectation; see Fig. 25f. The experimental data also show that the hierarchy of adsorption strengths for xylenes is $p > o > m$.

A similar "bookshelf" structure is afforded by Co(BDP), and the snapshots in Fig. 26 would suggest that this MOF will also have the potential for separation of C8 hydrocarbon mixtures. Experimental investigations are necessary to verify this expectation.

For separation of ethane/ethene and propane/propene mixtures, a different strategy needs to be employed in which differences in both adsorption and diffusion characteristics are exploited in permeation across ZIF-7 and ZIF-8 membranes.[45–47]

6. Conclusions

With the aid of CBMC and MD simulations we have examined the characteristics of a wide variety of MOFs, ZIFs, and zeolites for separation of a variety of mixtures using either PSA or membrane units. The separation performances have been characterized by four different metrics: (1) the adsorption selectivity, S_{ads}, (2) the working capacity or delta loading, Δq, (3) diffusion selectivity, S_{diff}, and (4) membrane permeability, Π_i. The following major conclusions emerge from this study.

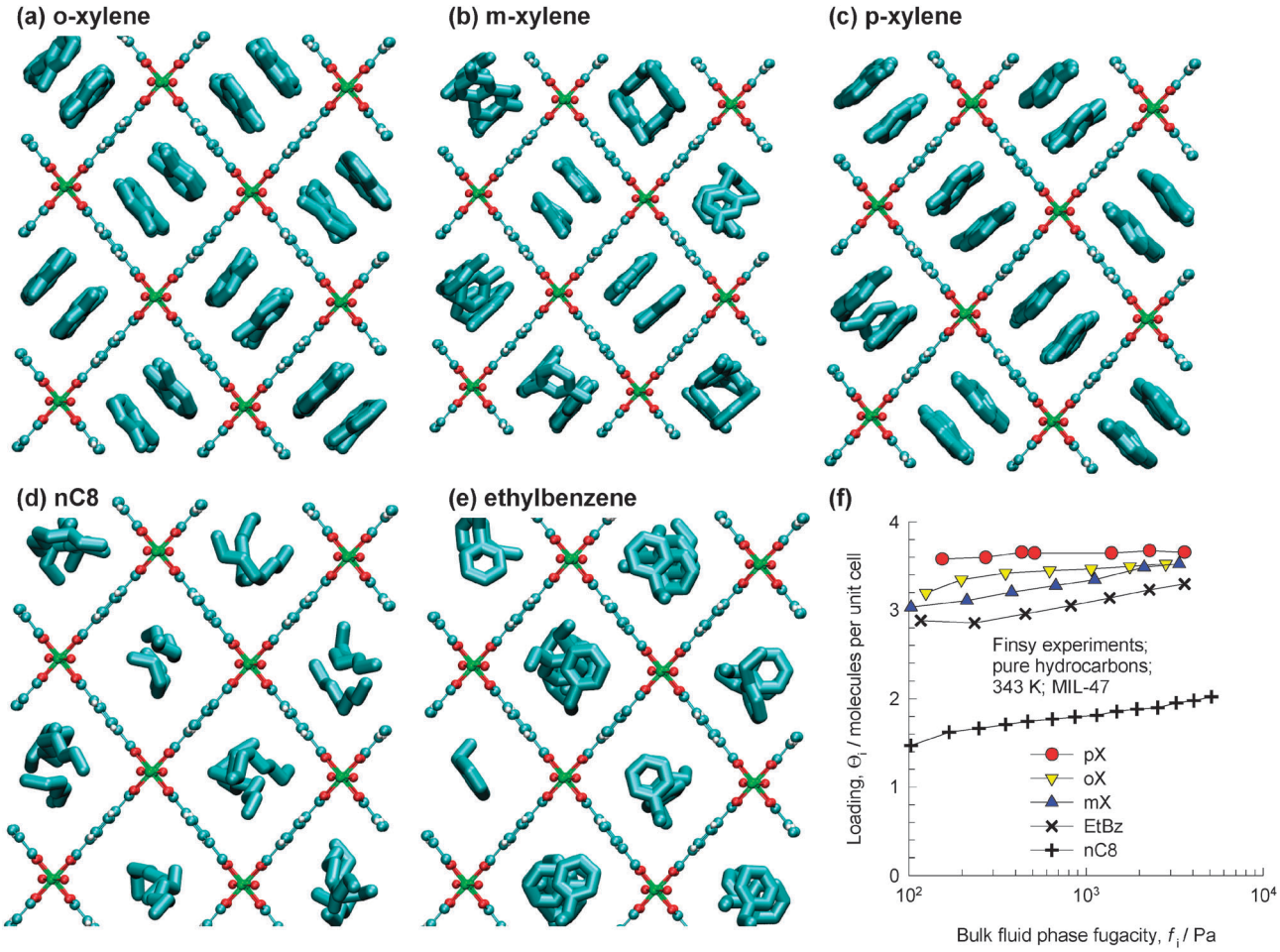

Fig. 25 Snapshots showing the location and conformations of (a) *o*-xylene, (b) *m*-xylene, (c) *p*-xylene, (d) *n*C8, and (e) ethylbenzene within the channels of MIL-47. (f) Experimental data on pure component isotherms for *n*-octane (*n*C8), ethyl-benzene (EtBz), *o*-, *m*-, and *p*-xylenes (*o*X, *m*X, *p*X) in MIL-47 at 343 K.[90]

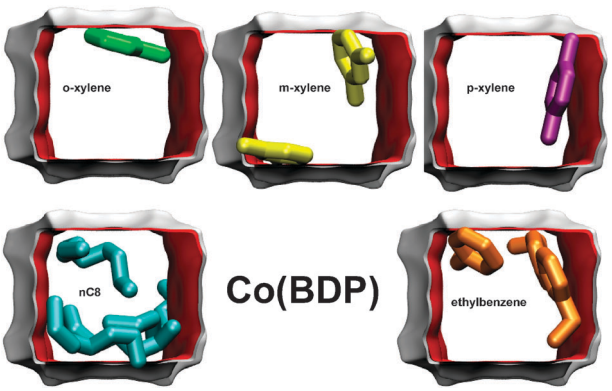

Fig. 26 Snapshots showing the location and conformations of *o*-xylene, *m*-xylene, *p*-xylene, *n*C8, and ethylbenzene within the channels of Co(BDP).

(1) Of all the MOFs investigated, the best CO_2 capture performance is obtained with MgMOF-74 that offers strong electrostatic interactions of CO_2 molecules with exposed metal cation sites. While traditional adsorbents such as NaX and NaY have higher S_{ads} values for CO_2/CH_4, CO_2/N_2, CO_2/H_2 separations, these suffer from relatively low working capacities that are important in PSA units. For CO_2/N_2, CO_2/H_2, and CH_4/H_2 separation in PSA units, MgMOF-74 is the MOF that offers the best combination of high S_{ads} values, concomitant with high working capacities Δq.

(2) Zeolites such as NaX, NaY, CHA, and DDR are often the preferred materials for use in membrane devices when high CO_2/CH_4 permeation selectivities are sought.

(3) For CO_2/H_2 and CO_2/N_2 separation, MgMOF-74 membranes offer both high permeabilities and permeation selectivities. These combined features may be attractive for practical exploitation, especially when upstream pressures exceed 1 MPa.[140]

(4) For CH_4/H_2 separation, ZnMOF-74 and MgMOF-74 membranes are CH_4-selective and of potential practical interest.

(5) For separation of hexane isomers, Co(BDP) offers both selectivity and capacity advantages over MFI zeolite that is currently considered to be the leading candidate for use in PSA units. The separation principle relies on the degree of "flatness" of molecular configurations; a flatter molecule can have better interactions with the framework.

(6) The relative degrees of flatness of molecules can be exploited for separation of xylenes from a C8 hydrocarbon mixture. For this purpose MOFs with bookshelf-like structures such as Co(BDP), and MIL-47 are suitable.

This perspective has underlined the many advantages of using molecular simulation tools for screening a wide variety of MOFs and zeolites. Such screening exercises can be expected to significantly reduce process development times.

Nomenclature

b_i	dual-Langmuir–Freundlich constant for species i, $Pa^{-\nu_i}$
c_i	pore concentration of species i, mol m^{-3}
$c_{i,sat}$	saturation pore concentration of species i, mol m^{-3}
c_t	total concentration in mixture, mol m^{-3}
$D_{i,self}$	self-diffusivity of species i, m^2 s^{-1}
f_i	fluid phase fugacity of species i, Pa
f_t	total bulk fluid phase fugacity of mixture, Pa
ℓ	thickness of microporous membrane layer, m
$-\Delta H_{st}$	isosteric heat of adsorption, J mol^{-1}
M_i	molar mass of species i, kg mol^{-1}
N_i	molar flux of species i, based on membrane area, mol m^{-2} s^{-1}
q_i	component molar loading of species i, mol kg^{-1}
$q_{i,sat}$	saturation loading of species i, mol kg^{-1}
q_i	total molar loading of mixture, mol kg^{-1}
Δq	delta loading or working capacity, mol kg^{-1}
S_{ads}	adsorption selectivity, dimensionless
S_{diff}	diffusion selectivity, dimensionless
S_{perm}	permeation selectivity, dimensionless
V_p	accessible pore volume, m^3 kg^{-1}
Greek letters	
ϕ	fractional pore volume, dimensionless
ν_i	exponent in the dual-Langmuir–Freundlich isotherm, dimensionless
Δf_i	differences in the partial fugacities between upstream and downstream membrane compartments, mol kg^{-1}
Π_i,	permeability of species i across membrane, mol m^{-1} s^{-1} Pa^{-1}
Subscripts	
A	referring to adsorption site A
B	referring to adsorption site B
i	referring to component i
t	referring to total mixture
sat	referring to saturation conditions

Acknowledgements

This material is based upon work supported as part of the Center for Gas Separations Relevant to Clean Energy Technologies, an Energy Frontier Research Center funded by the U.S. Department of Energy, Office of Science, Office of Basic Energy Sciences under Award Number DE-SC0001015.

References

1 M. Eddaoudi, J. Kim, N. Rosi, D. Vodak, J. Wachter, M. O'Keeffe and O. M. Yaghi, *Science*, 2002, **295**, 469–472.
2 R. Banerjee, H. Furukawa, D. Britt, C. Knobler, M. O'Keeffe and O. M. Yaghi, *J. Am. Chem. Soc.*, 2009, **131**, 3875–3877.
3 R. Banerjee, A. Phan, B. Wang, C. Knobler, H. Furukawa, M. O'Keeffe and O. M. Yaghi, *Science*, 2008, **319**, 939–943.
4 A. P. Côté, A. I. Benin, N. W. Ockwig, M. O'Keeffe, A. J. Matzger and O. M. Yaghi, *Science*, 2005, **310**, 1166–1170.
5 A. U. Czaja, N. Trukhan and U. Müller, *Chem. Soc. Rev.*, 2009, **38**, 1284–1293.
6 J. Y. Lee, O. K. Farha, J. Roberts, K. A. Scheidt, S. T. Nguyen and J. T. Hupp, *Chem. Soc. Rev.*, 2009, **38**, 1450–1459.
7 R. J. Kuppler, D. J. Timmons, Q. R. Fang, J. R. Li, T. A. Makal, M. D. Young, D. Yuan, D. Zhao, W. Zhuang and H. C. Zhou, *Coord. Chem. Rev.*, 2009, **253**, 3042–3066.
8 K. A. Cychosz, R. Ahmad and A. J. Matzger, *Chem. Sci.*, 2010, **1**, 293–302.
9 L. Ma and W. Lin, *Top. Curr. Chem.*, 2010, **293**, 175–205.
10 S. T. Meek, J. A. Greathouse and M. D. Allendorf, *Adv. Mater.*, 2011, **23**, 249–267.
11 G. Férey, C. Serre, T. Devic, G. Maurin, H. Jobic, P. L. Llewellyn, G. De Weireld, A. Vimont, M. Daturi and J. S. Chang, *Chem. Soc. Rev.*, 2011, **40**, 550–562.
12 J. R. Li, R. J. Kuppler and H. C. Zhou, *Chem. Soc. Rev.*, 2009, **38**, 1477–1504.
13 S. Keskin, T. M. van Heest and D. S. Sholl, *ChemSusChem*, 2010, **3**, 879–891.
14 D. M. D'Alessandro, B. Smit and J. R. Long, *Angew. Chem., Int. Ed.*, 2010, **49**, 6058–6082.
15 R. Krishna and J. M. van Baten, *J. Membr. Sci.*, 2010, **360**, 323–333.
16 M. T. Ho, G. W. Allinson and D. E. Wiley, *Ind. Eng. Chem. Res.*, 2008, **47**, 4883–4890.
17 C. Lastoskie, *Science*, 2010, **330**, 595–596.
18 Z. Bao, L. Yu, Q. Ren, X. Lu and S. Deng, *J. Colloid Interface Sci.*, 2011, **353**, 549–556.
19 Q. Wang, J. Luo, Z. Zhong and A. Borgna, *Energy Environ. Sci.*, 2011, **4**, 42–55.
20 L. Hamon, E. Jolimaitre and G. Pirngruber, *Ind. Eng. Chem. Res.*, 2010, **49**, 7497–7503.
21 N. Hedin, L. Chen and A. Laaksonen, *Nanoscale*, 2010, **2**, 1819–1841.
22 D. Zhao, D. J. Timmons, D. Yuan and H. Zhou, *Acc. Chem. Res.*, 2011, **44**, 123–133.
23 J. An and N. L. Rosi, *J. Am. Chem. Soc.*, 2010, **132**, 5578–5579.
24 R. Babarao and J. Jiang, *J. Am. Chem. Soc.*, 2009, **131**, 11417–11425.
25 D. Britt, H. Furukawa, B. Wang, T. G. Glover and O. M. Yaghi, *Proc. Natl. Acad. Sci. U. S. A.*, 2009, **106**, 20637–20640.
26 S. R. Caskey, A. G. Wong-Foy and A. J. Matzger, *J. Am. Chem. Soc.*, 2008, **130**, 10870–10871.
27 A. Ö. Yazaydın, A. I. Benin, S. A. Faheem, P. Jakubczak, J. J. Low, R. R. Willis and R. Q. Snurr, *Chem. Mater.*, 2009, **21**, 1425–1430.
28 A. Ö. Yazaydın, R. Q. Snurr, T. H. Park, K. Koh, J. Liu, M. D. LeVan, A. I. Benin, P. Jakubczak, M. Lanuza, D. B. Galloway, J. J. Low and R. R. Willis, *J. Am. Chem. Soc.*, 2009, **131**, 18198–18199.
29 Z. R. Herm, J. A. Swisher, B. Smit, R. Krishna and J. R. Long, *J. Am. Chem. Soc*, 2011, **133**, 5664–5667.
30 Y. S. Bae, O. K. Farha, J. T. Hupp and R. Q. Snurr, *J. Mater. Chem.*, 2009, **19**, 2131–2134.
31 B. Arstad, H. Fjellvåg, K. O. Kongshaug, O. Swang and R. Blom, *Adsorption*, 2008, **14**, 755–762.
32 R. Vaidhyanathan, S. S. Iremonger, K. W. Dawson and G. K. H. Shimizu, *Chem. Commun.*, 2009, 5230–5232.
33 A. Torrisi, C. Mellot-Draznieks and R. G. Bell, *J. Chem. Phys.*, 2009, **130**, 194703.
34 J. An, S. J. Geib and N. L. Rosi, *J. Am. Chem. Soc.*, 2010, **132**, 38–39.
35 A. Torrisi, R. G. Bell and C. Mellot-Draznieks, *Cryst. Growth Des.*, 2010, **10**, 2839–2841.
36 A. Demessence, D. M. D'Alessandro, M. W. Foo and J. R. Long, *J. Am. Chem. Soc.*, 2009, **131**, 8784–8786.
37 S. Couck, J. F. M. Denayer, G. V. Baron, T. Rémy, J. Gascon and F. Kapteijn, *J. Am. Chem. Soc.*, 2009, **131**, 6326–6327.
38 H. Deng, C. J. Doonan, H. Furukawa, R. B. Ferreira, J. John Towne, C. B. Knobler, B. Wang and O. M. Yaghi, *Science*, 2010, **327**, 846–850.

39 J. R. Karra and K. S. Walton, *J. Phys. Chem. C*, 2010, **114**, 15735–15740.
40 H. Bux, F. Liang, Y. Li, J. Cravillon, M. Wiebcke and J. Caro, *J. Am. Chem. Soc.*, 2009, **131**, 16000–16001.
41 Y. Li, F. Liang, H. Bux, W. Yang and J. Caro, *J. Membr. Sci.*, 2010, **354**, 48–54.
42 S. Keskin, *Ind. Eng. Chem. Res.*, 2010, **49**, 11689–11696.
43 M. Gallo and D. Glossman-Mitnik, *J. Phys. Chem. C*, 2009, **113**, 6634–6642.
44 S. Keskin, *J. Phys. Chem. C*, 2010, **114**, 13047–13054.
45 K. Li, D. H. Olson, J. Seidel, T. J. Emge, H. Gong, H. Zeng and J. Li, *J. Am. Chem. Soc.*, 2009, **131**, 10368–10369.
46 C. Gücüyener, J. van den Bergh, J. Gascon and F. Kapteijn, *J. Am. Chem. Soc.*, 2010, **132**, 17704–17706.
47 H. Bux, C. Chmelik, R. Krishna and J. Caro, *J. Membr. Sci.*, 2011, **369**, 284–289.
48 R. Krishna and J. M. van Baten, *Mol. Simul.*, 2009, **35**, 1098–1104.
49 K. Li, D. H. Olson, J. Y. Lee, W. Bi, K. Wu, T. Yuen, Q. Xu and J. Li, *Adv. Funct. Mater.*, 2008, **18**, 2205–2214.
50 B. Chen, C. Liang, J. Yang, D. S. Contreras, Y. L. Clancy, E. B. Lobkovsky, O. M. Yaghi and S. Dai, *Angew. Chem., Int. Ed.*, 2006, **45**, 1590–1595.
51 J. Jiang and S. I. Sandler, *Langmuir*, 2006, **22**, 5702–5707.
52 R. Krishna and J. M. van Baten, *Langmuir*, 2010, **26**, 8450–8463.
53 R. Babarao, Y. H. Tong and J. Jiang, *J. Phys. Chem. B*, 2009, **113**, 9129–9136.
54 D. Dubbeldam, C. J. Galvin, K. S. Walton, D. E. Ellis and R. Q. Snurr, *J. Am. Chem. Soc.*, 2008, **130**, 10884–10885.
55 Z. Y. Gu and X. P. Yan, *Angew. Chem., Int. Ed.*, 2010, **49**, 1477–1480.
56 Z. Y. Gu, D. Q. Jiang, H. F. Wang, X. Y. Cui and X. P. Yan, *J. Phys. Chem. C*, 2010, **114**, 311–316.
57 J. M. Castillo, T. J. H. Vlugt and S. Calero, *J. Phys. Chem. C*, 2009, **113**, 20869–20874.
58 T. G. Glover, G. W. Peterson, B. J. Schindler, D. Britt and O. Yaghi, *Chem. Eng. Sci.*, 2011, **66**, 163–170.
59 H. Bux, C. Chmelik, J. M. Van Baten, R. Krishna and J. Caro, *Adv. Mater.*, 2010, **22**, 4741–4743.
60 M. Palomino, A. Corma and F. Rey, *Langmuir*, 2010, **26**, 1910–1917.
61 R. Krishna and J. R. Long, *J. Phys. Chem. C*, 2011http://dx.doi.org/10.1021/jp102203c.
62 R. Kumar, *Ind. Eng. Chem. Res.*, 1994, **33**, 1600–1605.
63 R. Krishna, *J. Phys. Chem. C*, 2009, **113**, 19756–19781.
64 R. Krishna and J. M. van Baten, *Chem. Eng. Sci.*, 2008, **63**, 3120–3140.
65 R. Krishna and J. M. van Baten, *Microporous Mesoporous Mater.*, 2008, **109**, 91–108.
66 R. Krishna and J. M. van Baten, *Chem. Eng. Sci.*, 2009, **64**, 3159–3178.
67 R. Krishna and R. Baur, *Sep. Purif. Technol.*, 2003, **33**, 213–254.
68 R. Krishna and D. Paschek, *Sep. Purif. Technol.*, 2000, **21**, 111–136.
69 R. Krishna and J. M. van Baten, *J. Membr. Sci.*, 2011, **367**, 204–210.
70 Q. Yang and C. Zhong, *J. Phys. Chem. B*, 2006, **110**, 17776–17783.
71 S. Keskin and D. S. Sholl, *Langmuir*, 2009, **25**, 11786–11795.
72 S. Keskin and D. S. Sholl, *Energy Environ. Sci.*, 2010, **3**, 343–351.
73 R. Krishna and J. M. van Baten, *Sep. Purif. Technol.*, 2007, **55**, 246–255.
74 R. Krishna and J. M. van Baten, *Chem. Eng. J.*, 2007, **133**, 121–131.
75 Y. C. Liu, D. Liu, Q. Yang, C. Zhong and J. Mi, *Ind. Eng. Chem. Res.*, 2010, **49**, 2902–2906.
76 R. Q. Snurr, A. Ö. Yazaydın, D. Dubbeldam and H. Frost, in *Metal–Organic Frameworks: Design and Application*, ed. L. R. MacGillivray, John Wiley & Sons, Hoboken, N.J., 2010, pp. 313–339.
77 D. Liu and C. Zhong, *J. Mater. Chem.*, 2010, **20**, 10308–10318.
78 T. Düren, Y. S. Bae and R. Q. Snurr, *Chem. Soc. Rev.*, 2009, **38**, 1237–1247.
79 R. Krishna and J. M. van Baten, *Langmuir*, 2010, **26**, 2975–2978.
80 Q. Yang, L. Ma, C. Zhong, X. An and D. Liu, *J. Phys. Chem. C*, 2011, **115**, 2790–2797.
81 N. L. Rosi, J. Kim, M. Eddaoudi, B. Chen, M. O'Keeffe and O. M. Yaghi, *J. Am. Chem. Soc.*, 2005, **127**, 1504–1518.
82 P. D. C. Dietzel, B. Panella, M. Hirscher, R. Blom and H. Fjellvåg, *Chem. Commun.*, 2006, 959–961.
83 P. D. C. Dietzel, V. Besikiotis and R. Blom, *J. Mater. Chem.*, 2009, **19**, 7362–7370.
84 H. K. Chae, D. Y. Siberio-Pérez, J. Kim, Y. B. Go, M. Eddaoudi, A. J. Matzger, M. O'Keeffe and O. M. Yaghi, *Nature*, 2004, **427**, 523–527.
85 C. Chmelik, J. Kärger, M. Wiebcke, J. Caro, J. M. van Baten and R. Krishna, *Microporous Mesoporous Mater.*, 2009, **117**, 22–32.
86 D. Dubbeldam, K. S. Walton, D. E. Ellis and R. Q. Snurr, *Angew. Chem., Int. Ed.*, 2007, **46**, 4496–4499.
87 D. Dubbeldam, H. Frost, K. S. Walton and R. Q. Snurr, *Fluid Phase Equilib.*, 2007, **261**, 152–161.
88 D. S. Coombes, F. Corà, C. Mellot-Draznieks and R. G. Bell, *J. Phys. Chem. C*, 2009, **113**, 544–552.
89 L. Alaerts, C. E. A. Kirschhock, M. Maes, M. van der Veen, V. Finsy, A. Depla, J. A. Martens, G. V. Baron, P. A. Jacobs, J. F. M. Denayer and D. De Vos, *Angew. Chem., Int. Ed.*, 2007, **46**, 4293–4297.
90 V. Finsy, H. Verelst, L. Alaerts, D. De Vos, P. A. Jacobs, G. V. Baron and J. F. M. Denayer, *J. Am. Chem. Soc.*, 2008, **130**, 7110–7118.
91 K. Barthelet, J. Marrot, D. Riou and G. Férey, *Angew. Chem., Int. Ed.*, 2007, **41**, 281–284.
92 P. S. Bárcia, F. Zapata, J. A. C. Silva, A. E. Rodrigues and B. Chen, *J. Phys. Chem. B*, 2008, **111**, 6101–6103.
93 J. Y. Lee, D. H. Olson, L. Pan, T. J. Emge and J. Li, *Adv. Funct. Mater.*, 2007, **17**, 1255–1262.
94 K. Sumida, M. R. Hill, S. Horike, A. Dailly and J. R. Long, *J. Am. Chem. Soc.*, 2009, **131**, 15120–15121.
95 H. J. Choi, M. Dincă and J. R. Long, *J. Am. Chem. Soc.*, 2008, **130**, 7848–7850.
96 F. Salles, G. Maurin, C. Serre, P. L. Llewellyn, C. Knöfel, H. J. Choi, Y. Filinchuk, L. Oliviero, A. Vimont, J. R. Long and G. Férey, *J. Am. Chem. Soc.*, 2010, **132**, 13782–13788.
97 C. Baerlocher and L. B. McCusker, Database of Zeolite Structures, International Zeolite Association, http://www.iza-structure.org/databases/, 10 January 2002.
98 T. J. H. Vlugt, R. Krishna and B. Smit, *J. Phys. Chem. B*, 1999, **103**, 1102–1118.
99 A. H. Fuchs and A. K. Cheetham, *J. Phys. Chem. B*, 2001, **105**, 7375–7383.
100 R. Krishna, B. Smit and S. Calero, *Chem. Soc. Rev.*, 2002, **31**, 185–194.
101 D. Dubbeldam and R. Q. Snurr, *Mol. Simul.*, 2007, **33**, 15–30.
102 B. Smit and T. L. M. Maesen, *Chem. Rev.*, 2008, **108**, 4125–4184.
103 S. Keskin, J. Liu, R. B. Rankin, J. K. Johnson and D. S. Sholl, *Ind. Eng. Chem. Res.*, 2009, **48**, 2355–2371.
104 K. E. Gubbins, Y. C. Liu, J. D. Moore and J. C. Palmer, *Phys. Chem. Chem. Phys.*, 2011, **13**, 58–85.
105 P. Ungerer, B. Tavitian and A. Boutin, *Simulation in the Oil and Gas Industry. Monte Carlo Methods*, Editions Technip, Paris, 2005.
106 D. Frenkel and B. Smit, *Understanding Molecular Simulations: From Algorithms to Applications*, Academic Press, San Diego, 2nd edn, 2002.
107 D. S. Sholl and J. A. Stechel, *Density Functional Theory. A Practical Introduction*, John Wiley, Hoboken, N.J., 2009.
108 D. Dubbeldam, S. Calero, T. J. H. Vlugt, R. Krishna, T. L. M. Maesen and B. Smit, *J. Phys. Chem. B*, 2004, **108**, 12301–12313.
109 S. Calero, D. Dubbeldam, R. Krishna, B. Smit, T. J. H. Vlugt, J. F. M. Denayer, J. A. Martens and T. L. M. Maesen, *J. Am. Chem. Soc.*, 2004, **126**, 11377–11386.
110 E. García-Pérez, J. B. Parra, C. O. Ania, A. García-Sánchez, J. M. Van Baten, R. Krishna, D. Dubbeldam and S. Calero, *Adsorption*, 2007, **13**, 469–476.
111 A. García-Sánchez, C. O. Ania, J. B. Parra, D. Dubbeldam, T. J. H. Vlugt, R. Krishna and S. Calero, *J. Phys. Chem. C*, 2009, **113**, 8814–8820.

112 A. K. Rappé, C. J. Casewit, K. S. Colwel, W. A. Goddard and W. M. Skiff, *J. Am. Chem. Soc.*, 1992, **114**, 10024–10035.
113 S. L. Mayo, B. D. Olafson and W. A. Goddard, *J. Phys. Chem.*, 1990, **94**, 8897–8909.
114 N. Rosenbach, H. Jobic, A. Ghoufi, F. Salles, G. Maurin, S. Bourrelly, P. L. Llewellyn, T. Devic, C. Serre and G. Férey, *Angew. Chem., Int. Ed.*, 2008, **47**, 6611–6615.
115 F. Salles, A. Ghoufi, G. Maurin, R. G. Bell, C. Mellot-Draznieks and G. Férey, *Angew. Chem., Int. Ed.*, 2008, **47**, 8487–8491.
116 R. B. Rankin, J. Liu, A. D. Kulkarni and J. K. Johnson, *J. Phys. Chem. C*, 2009, **113**, 16906–16914.
117 Q. Xu and C. Zhong, *J. Phys. Chem. C*, 2010, **114**, 5035–5042.
118 C. Zheng and C. Zhong, *J. Phys. Chem. C*, 2010, **114**, 9945–9951.
119 L. Heinke, D. Tzoulaki, C. Chmelik, F. Hibbe, J. M. van Baten, H. Lim, J. Li, R. Krishna and J. Kärger, *Phys. Rev. Lett.*, 2009, **102**, 065901.
120 D. Tzoulaki, L. Heinke, H. Lim, J. Li, D. Olson, J. Caro, R. Krishna, C. Chmelik and J. Kärger, *Angew. Chem., Int. Ed.*, 2009, **48**, 3525–3528.
121 P. Demontis and G. B. Suffritti, *Microporous Mesoporous Mater.*, 2009, **125**, 160–168.
122 K. Seehamart, T. Nanok, J. Kärger, C. Chmelik, R. Krishna and S. Fritzsche, *Microporous Mesoporous Mater.*, 2010, **130**, 92–96.
123 K. Seehamart, T. Nanok, R. Krishna, J. M. van Baten, T. Remsungnen and S. Fritzsche, *Microporous Mesoporous Mater.*, 2009, **125**, 97–100.
124 K. Seehamart, C. Chmelik, R. Krishna and S. Fritzsche, *Microporous Mesoporous Mater.*, 2011, http://dx.doi.org/10.1016/j.micromeso.2011.02.018.
125 D. Dubbeldam, R. Krishna and R. Q. Snurr, *J. Phys. Chem. C*, 2009, **113**, 19317–19327.
126 R. Krishna and J. M. van Baten, *J. Phys. Chem. C*, 2010, **114**, 18017–18021.
127 R. Krishna and J. M. van Baten, *Microporous Mesoporous Mater.*, 2011, **137**, 83–91.
128 C. Serre, F. Millange, C. Thouvenot, M. Nouguès, G. Marsolier, D. Louër and G. Férey, *J. Am. Chem. Soc.*, 2002, **124**, 13519–13526.
129 B. Liu and B. Smit, *Langmuir*, 2009, **25**, 5918–5926.
130 R. Krishna and J. M. van Baten, *Sep. Purif. Technol.*, 2008, **61**, 414–423.
131 R. Krishna and J. M. van Baten, *Langmuir*, 2010, **26**, 3981–3992.
132 R. Krishna and J. M. van Baten, *Chem. Phys. Lett.*, 2007, **446**, 344–349.
133 R. Krishna and J. M. van Baten, *Langmuir*, 2010, **26**, 10854–10867.
134 B. Liu and B. Smit, *J. Phys. Chem. C*, 2010, **114**, 8515–8522.
135 O. Talu, *Adv. Colloid Interface Sci.*, 1998, **77**, 227–269.
136 A. L. Myers and J. M. Prausnitz, *AIChE J.*, 1965, **11**, 121–130.
137 R. Krishna, S. Calero and B. Smit, *Chem. Eng. J.*, 2002, **88**, 81–94.
138 R. Krishna and J. M. van Baten, *Microporous Mesoporous Mater.*, 2011, **142**, 745–748.
139 R. Krishna and J. M. van Baten, *Microporous Mesoporous Mater.*, 2011, **138**, 228–234.
140 R. Krishna and J. M. van Baten, *J. Membr. Sci.*, 2011, submitted for publication.
141 R. Krishna and J. M. van Baten, *Chem. Eng. Sci.*, 2009, **64**, 870–882.
142 R. Krishna and J. M. van Baten, *J. Membr. Sci.*, 2011, **369**, 545–549.
143 R. Krishna and J. M. van Baten, *Ind. Eng. Chem. Res.*, 2011, http://dx.doi.org/10.1021/ie100277z.
144 R. Krishna and J. M. van Baten, *J. Phys. Chem. C*, 2010, **114**, 11557–11563.
145 L. M. Robeson, *J. Membr. Sci.*, 2008, **320**, 390–400.
146 S. Himeno, T. Tomita, K. Suzuki, K. Nakayama and S. Yoshida, *Ind. Eng. Chem. Res.*, 2007, **46**, 6989–6997.
147 J. van den Bergh, W. Zhu, J. Gascon, J. A. Moulijn and F. Kapteijn, *J. Membr. Sci.*, 2008, **316**, 35–45.
148 R. Krishna, J. M. van Baten, E. García-Pérez and S. Calero, *Ind. Eng. Chem. Res.*, 2007, **46**, 2974–2986.
149 R. Krishna, S. Li, J. M. van Baten, J. L. Falconer and R. D. Noble, *Sep. Purif. Technol.*, 2008, **60**, 230–236.
150 S. Li, J. L. Falconer, R. D. Noble and R. Krishna, *Ind. Eng. Chem. Res.*, 2007, **46**, 3904–3911.
151 S. Li, J. L. Falconer, R. D. Noble and R. Krishna, *J. Phys. Chem. C*, 2007, **111**, 5075–5082.
152 K. Kusakabe, T. Kuroda, A. Murata and S. Morooka, *Ind. Eng. Chem. Res.*, 1997, **36**, 649–655.
153 Y. Hasegawa, T. Tanaka, K. Watanabe, B. H. Jeong, K. Kusakabe and S. Morooka, *Korean J. Chem. Eng.*, 2002, **19**, 309–313.
154 Y. Hasegawa, K. Watanabe, K. Kusakabe and S. Morooka, *J. Membr. Sci.*, 2002, **208**, 415–418.
155 J. C. White, P. K. Dutta, K. Shqau and H. Verweij, *Langmuir*, 2010, **26**, 10287–10293.
156 Y. S. Li, F. Y. Liang, H. Bux, A. Veldhoff, W. S. Yang and J. Caro, *Angew. Chem., Int. Ed.*, 2010, **49**, 548–551.
157 R. W. Carr and H. W. Dandekar, in *Reactive Separation Processes*, ed. S. Kulprathipanja, Taylor & Francis, New York, USA, 2nd edn, 2001, pp. 115–154.
158 H. W. Dandekar, G. A. Funk, R. D. Gillespie, H. A. Zinnen, C. P. McGonegal, M. Kojima and S. H. Hobbs, *Process for alkane isomerization using reactive chromatography, UOP Inc., USA., US Pat., US 5763730*, 1998.
159 H. W. Dandekar, G. A. Funk and H. A. Zinnen, *Process for separating and recovering multimethyl-branched alkanes, UOP Inc., USA., U.S. Pat., US 6069289*, 2000.
160 R. Krishna, *Chem. Eng. Res. Des.*, 2001, **79**, 182–194.
161 S. Calero, B. Smit and R. Krishna, *Phys. Chem. Chem. Phys.*, 2001, **3**, 4390–4398.
162 S. Calero, B. Smit and R. Krishna, *J. Catal.*, 2001, **202**, 395–401.
163 R. Krishna and R. Baur, *Chem. Eng. Sci.*, 2005, **60**, 1155–1166.
164 R. Baur and R. Krishna, *Chem. Eng. J.*, 2005, **109**, 107–113.
165 E. Jolimaître, K. Ragil, M. Tayakout-Fayolle and C. Jallut, *AIChE J.*, 2002, **48**, 1927–1937.
166 P. S. Bárcia, D. Guimarães, P. A. P. Mendes, J. A. C. Silva, V. Guillerm, H. Chevreau, C. Serre and A. E. Rodrigues, *Microporous Mesoporous Mater.*, 2011, **139**, 67–73.
167 J. M. van Baten and R. Krishna, *Microporous Mesoporous Mater.*, 2005, **84**, 179–191.
168 B. L. Severson and R. Q. Snurr, *J. Chem. Phys.*, 2007, **126**, 134708.

